Loop induced $H^{\pm} \to W^{\pm}Z$ decays in the aligned two-Higgs-doublet model

Gauhar Abbas,[1,*] Diganta Das,[2,†] and Monalisa Patra[3,‡]

[1]Department of Physics, Indian Institute of Technology (BHU), Varanasi 221005, India
[2]Department of Physics and Astrophysics, University of Delhi, Delhi 110007, India
[3]Jožef Stefan Institute, Jamova 39, P. O. Box 3000, 1001 Ljubljana, Slovenia

(Received 28 August 2018; published 7 December 2018)

We present a complete one-loop computation of the $H^{\pm} \to W^{\pm}Z$ decay in the aligned two-Higgs-doublet model. The constraints from the electroweak precision observables, perturbative unitarity, vacuum stability, and flavor physics are all taken into account along with the latest Large Hadron Collider searches for the charged Higgs. It is observed that a large enhancement of the branching ratio can be obtained in the limit where there is a large splitting between the charged and pseudoscalar Higgs masses as well as for the largest allowed values of the alignment parameter ς_u. We find that the maximum possible branching ratio in the case of a large mass splitting between $m_{H^{\pm}}$ and m_A is $\approx 10^{-3}$ for $m_{H^{\pm}} \in (200, 700)$ GeV.

DOI: 10.1103/PhysRevD.98.115013

I. INTRODUCTION

Following the discovery of a Higgs-like particle at the Large Hadron Collider, we are a step closer to understanding the electroweak symmetry breaking (EWSB) mechanism in the Standard Model (SM). This discovery, however, raises one important question: that is, whether the Higgs-like particle is indeed the Higgs of the SM or a component of an extended scalar sector corresponding to a richer EWSB scenario than in the SM. One of the simplest beyond SM scenarios is the two-Higgs-doublet model (2HDM) in which the SM Higgs doublet is supplemented with one additional scalar doublet [1,2]. There are many motivations to introduce extra Higgs doublets, for example, to explain the electroweak baryogenesis [3], top-bottom mass hierarchy [4], and neutrino mass generation [5], to name a few. The discerning feature of the extension with one extra Higgs doublet is that it leads to four additional scalar particles beyond the SM, namely, two charged scalars and two neutral scalars. Various properties of these additional scalars can be probed through precise determinations of the Higgs properties such as its mass, production cross section, and decays involving the SM-like Higgs [6]. The direct searches of these scalar particles at the LHC could help us in acquiring an understanding of the scalar sector of a more fundamental underlying theory.

The charged Higgs ($H^{\pm}$) is one of the new particles of the extended Higgs sector of the 2HDM, and if such particle exists, its direct detection could lead us to a better understanding of the extended scalar sector. The charged Higgs is currently been searched at the LHC through different production and decay modes [7]. The tb decay mode is considered in the search of a heavy charged Higgs, whereas the preferred decay mode channel for light charged Higgs searches is the $\tau\nu_\tau$ channel.

Among the various decay channels of the charged Higgs, the $W^{\mp}Z$ decay mode is quite interesting because the $H^{\pm}W^{\mp}Z$ vertex does not occur at tree level in general multi-Higgs doublet models, in contrast to more exotic scalar sectors (e.g., triplets) in which this decay can occur at tree level [8–11]. The absence of this tree-level vertex is due to the weak isospin symmetry of the scalar kinetic terms [12,13]. The $H^{\pm}W^{\pm}Z$ vertex in 2HDM is therefore loop induced; however, it is well known that an observable enhancement in the magnitude of the vertex can come from nondecoupling effects of particles running in the loop. These are, in particular, the interactions that break custodial symmetry; for instance, the top and bottom quark-loop contributions to the $H^{\pm}W^{\pm}Z$ vertex show a quadratic dependence on the top quark mass [14].[1] In the context of 2HDM of type II, it is shown in Refs. [15,16] that an enhancement of $H^{\pm} \to W^{\pm}Z$ is possible due to the nondecoupling effect of the heavy Higgs bosons, i.e., a large mass difference between the CP-odd neutral scalars and the charged Higgs that breaks the custodial symmetry.

*gauhar.phy@iitbhu.ac.in
†diganta99@gmail.com
‡monalisa.patra@ijs.si

[1]The multi-Higgs doublet model being $U(1)_{em}$ symmetric, the vertex $H^{\pm}W^{\mp}\gamma$ is also loop induced and receives only logarithmic mass effects. Therefore, the $H^{\pm} \to W^{\pm}\gamma$ amplitude is not sensitive to the nondecoupling effects.

Thus, the $H^\pm W^\pm Z$ vertex has nontrivial consequences in the context of custodial symmetry. This decay channel has been studied in the context of three Higgs doublet models [17] as well as with in the effective Lagrangian extension of the 2HDMs [18] and minimal supersymmetric standard model [19].

In the most general version of 2HDMs, there are large flavor changing neutral current (FCNC) interactions that are in conflict with various flavor data. This problem is usually avoided by the natural flavor conservation hypothesis, implementing a discrete Z_2 symmetry that allows only one scalar field to couple to a given type of right-handed fermion [20,21], and hence evades tree-level FCNC. In the aligned two-Higgs-doublet model (A2HDM), the FCNC problem is solved in a more general way by aligning the Yukawa matrices in the flavor space [22]. It is based on the assumption that the Yukawa matrices coupled to a given right-handed fermion have the same flavor structure. These matrices can then be diagonalized simultaneously leading to no FCNCs at tree level. The scalar sector in the A2HDM is similar to the scalar sector of the most general 2HDMs, whereas the Yukawa sector is parametrized in terms of three complex couplings $\varsigma_{u,d,\ell}$, known as the alignment parameters. The A2HDM can be considered as a relatively general framework, from which all the known versions of the 2HDMs can be recovered under different limits of the alignment parameters. Phenomenological analyses of the A2HDM taking into account the latest LHC results and flavor physics observables can be found in Refs. [23–42].

In this work, we study the $H^\pm \to W^\pm Z$ decay within the framework of the *CP*-conserving A2HDM. We take into account the most recent limits from the LHC along with theoretical constraints such as vacuum stability, perturbative unitarity, and experimental bounds from charged Higgs searches at LEP and flavor physics. In the case of the 2HDM of type II, it was shown that with the soft-breaking parameter being small a large mass difference between the charged and the *CP*-odd scalars in the nondecoupling limit leads to an enhanced contribution to the decay width from the scalar-loop diagrams [15,16]. However, in the A2HDM, the scalar-loop diagrams are proportional to the quartic couplings that are either independent parameters or are functions of masses. Therefore, a large value of these independent quartic couplings along with a large mass splitting in the Higgs sector leads to an enhanced contribution from the Higgs boson–loop diagrams in our case.

The paper is organized as follows. We briefly describe the A2HDM in Sec. II. The theoretical and experimental constraints on the parameter space of the A2HDM are discussed in Sec. III. We evaluate the decay $H^\pm \to W^\pm Z$ and the relevant branching ratios in the A2HDM in Sec. IV, and in Sec. V, we present the results of the LHC production cross section for the processes $gb \to H^+\bar{t}$ and single charged Higgs production through WZ fusion with the subsequent decay of $H^\pm$ to $W^\pm Z$. We finally summarize our results in Sec. VI. The analytical results of the various diagrams contributing to the decay amplitude are listed in the Appendices.

II. ALIGNED TWO-HIGGS DOUBLET MODEL

The two complex scalar doublets of the A2HDM in the Higgs basis, in which only one doublet acquires a vacuum expectation value, can be written as [22]

$$\Phi_1 = \begin{bmatrix} G^+ \\ \frac{1}{\sqrt{2}}(v + S_1 + iG^0) \end{bmatrix}, \qquad \Phi_2 = \begin{bmatrix} H^+ \\ \frac{1}{\sqrt{2}}(S_2 + iS_3) \end{bmatrix}, \tag{1}$$

where $v = (\sqrt{2}G_F)^{-1/2} \simeq 246$ GeV, $G^{0,\pm}$ denote the would-be Goldstone bosons, and $H^\pm$ are the charged Higgs. The three neutral Higgs bosons are denoted by $\varphi_j^0(x) = \{h(x), H(x), A(x)\}$, and they are related to the S_i fields by the transformation $\varphi_j^0 = \mathcal{R}_{jk}S_k$. The $\mathcal{R}$ matrix is orthogonal and diagonalizes the mass terms in the scalar potential [32]. The most general scalar potential of the 2HDM is of the form

$$\begin{aligned} V = {} & \mu_1\Phi_1^\dagger\Phi_1 + \mu_2\Phi_2^\dagger\Phi_2 + [\mu_3\Phi_1^\dagger\Phi_2 + \mu_3^*\Phi_2^\dagger\Phi_1] \\ & + \lambda_1(\Phi_1^\dagger\Phi_1)^2 + \lambda_2(\Phi_2^\dagger\Phi_2)^2 + \lambda_3(\Phi_1^\dagger\Phi_1)(\Phi_2^\dagger\Phi_2) \\ & + \lambda_4(\Phi_1^\dagger\Phi_2)(\Phi_2^\dagger\Phi_1) + [(\lambda_5\Phi_1^\dagger\Phi_2 + \lambda_6\Phi_1^\dagger\Phi_1 \\ & + \lambda_7\Phi_2^\dagger\Phi_2)(\Phi_1^\dagger\Phi_2) + \text{H.c.}]. \end{aligned} \tag{2}$$

Because of Hermiticity, all parameters appearing in V are real except μ_3, λ_5, λ_6, and λ_7 that introduce additional source of *CP* violation. To reduce the number of independent parameters in our analysis, we limit ourselves to the *CP*-conserving case, so that μ_3, λ_5, λ_6, and λ_7 are real. The minimization of the scalar potential leads to the relations

$$\mu_1 = -\lambda_1 v^2, \qquad \mu_3 = -\frac{1}{2}\lambda_6 v^2, \tag{3}$$

with the charged Higgs mass being given by

$$m_{H^\pm}^2 = \mu_2 + \frac{1}{2}\lambda_3 v^2. \tag{4}$$

In the *CP*-conserving limit, the *CP*-odd field A directly corresponds to S_3, and the physical neutral Higgs bosons are related to S_1 and S_2 through the following transformation:

$$\begin{pmatrix} h \\ H \end{pmatrix} = \begin{bmatrix} \cos\tilde{\alpha} & \sin\tilde{\alpha} \\ -\sin\tilde{\alpha} & \cos\tilde{\alpha} \end{bmatrix} \begin{pmatrix} S_1 \\ S_2 \end{pmatrix}. \tag{5}$$

When $m_h \leq m_H$, the angle $\tilde{\alpha}$ is given by the following relations:

$$\sin 2\tilde{\alpha} = \frac{-2\lambda_6 v^2}{m_H^2 - m_h^2}, \quad \cos 2\tilde{\alpha} = \frac{m_A^2 + 2(\lambda_5 - \lambda_1)v^2}{m_H^2 - m_h^2}. \tag{6}$$

The range of the mixing angle $\tilde{\alpha}$ is constrained to $0 \le \tilde{\alpha} < \pi$ through a phase redefinition of the CP-even fields. The scalar masses in the CP-conserving limit are given as

$$m_h^2 = \frac{1}{2}(\Sigma - \Delta), \qquad m_H^2 = \frac{1}{2}(\Sigma + \Delta),$$
$$m_A^2 = m_{H^\pm}^2 + v^2\left(\frac{\lambda_4}{2} - \lambda_5\right), \tag{7}$$

with

$$\Sigma = m_{H^\pm}^2 + \left(2\lambda_1 + \frac{\lambda_4}{2} + \lambda_5\right)v^2,$$
$$\Delta = \sqrt{[m_A^2 + 2(\lambda_5 - \lambda_1)v^2]^2 + 4v^4\lambda_6^2}. \tag{8}$$

The Yukawa Lagrangian in the A2HDM in terms of the fermion mass eigenstates is written as [22]

$$\mathcal{L}_Y = -\frac{\sqrt{2}}{v}H^+\{\bar{u}[\varsigma_d V_{\rm CKM} m_d P_R - \varsigma_u m_u^\dagger V_{\rm CKM} P_L]d + \varsigma_\ell \bar{\nu} m_\ell P_R \ell\} - \frac{1}{v}\sum_{\varphi_i^0, f} y_f^{\varphi_i^0}\varphi_i^0[\bar{f} m_f P_R f] + \text{H.c.}, \tag{9}$$

where $P_{L,R} = (1 \mp \gamma_5)/2$ are the chirality projection operators, $m_{f=u,d,\ell}$ are the fermion masses, and $V_{\rm CKM}$ is the Cabibbo-Kobayashi-Maskawa (CKM) matrix element. The neutral Higgs couplings are given by

$$y_{d,\ell}^{\varphi_i^0} = \mathcal{R}_{i1} + (\mathcal{R}_{i2} + i\mathcal{R}_{i3})\varsigma_{d,\ell},$$
$$y_u^{\varphi_i^0} = \mathcal{R}_{i1} + (\mathcal{R}_{i2} - i\mathcal{R}_{i3})\varsigma_u^*. \tag{10}$$

The parameters ς_f $(f = u, d, \ell)$ represent alignment conditions in the flavor space and are family-universal complex quantities leading to new sources of CP violation beyond the CKM matrix. We consider these parameters to be real for our analysis. All the known versions of the 2HDM with natural flavor conservation can be recovered by taking particular limits of the aligned parameters as shown in Table I. The most stringent constraints on the modulus of the aligned parameters come from flavor physics to be discussed in the next sections.

TABLE I. The couplings ς_f in various types of two-Higgs-doublet models with Z_2 symmetry.

Model	ς_d	ς_u	ς_ℓ
Type I	$\cot\beta$	$\cot\beta$	$\cot\beta$
Type II	$-\tan\beta$	$\cot\beta$	$-\tan\beta$
Type X (lepton specific)	$\cot\beta$	$\cot\beta$	$-\tan\beta$
Type Y (flipped)	$-\tan\beta$	$\cot\beta$	$\cot\beta$

III. THEORETICAL AND EXPERIMENTAL CONSTRAINTS

In this section, we explore the various theoretical and experimental constraints on the parameter space of the CP-conserving A2HDM. In this limit, there are 11 real free parameters, which include μ_2, the couplings $\lambda_i (i = 1\ldots7)$, and the three alignment parameters $\varsigma_{u,d,\ell}$. Four of the parameters of the scalar potential can be expressed in terms of the physical scalar masses and the mixing angle $\tilde{\alpha}$ and are given by

$$\lambda_1 = \frac{1}{2v^2}(m_h^2\cos^2\tilde{\alpha} + m_H^2\sin^2\tilde{\alpha}),$$
$$\lambda_4 = \frac{1}{v^2}(m_h^2\sin^2\tilde{\alpha} + m_H^2\cos^2\tilde{\alpha} + m_A^2 - 2m_{H^\pm}^2), \tag{11}$$
$$\lambda_5 = \frac{1}{2v^2}(m_h^2\sin^2\tilde{\alpha} + m_H^2\cos^2\tilde{\alpha} - m_A^2),$$
$$\lambda_6 = -\frac{1}{v^2}(m_H^2 - m_h^2)\cos\tilde{\alpha}\sin\tilde{\alpha}. \tag{12}$$

Taking into account the above relations along with Eq. (4) leads us to work with a set of parameters that can be related to the physical masses m_h, m_A, m_H, $m_{H^\pm}$, the mixing parameter $\cos\tilde{\alpha}$, three couplings $\lambda_{2,3,7}$, and the Yukawa parameters $\varsigma_{u,d,\ell}$. We have fixed $m_h = 125.5$ GeV in our calculation with the assumption that the scalar boson observed by the ATLAS [43] and the CMS collaborations [44] corresponds to the lightest CP-even state h in the A2HDM. We also set $\cos\tilde{\alpha} = 0.95$ in order to ensure that the couplings of h to the gauge bosons, λ_{WW}^h and λ_{ZZ}^h, remain consistent with the LHC data.

The loop induced $h \to \gamma\gamma$ decay width receives a contribution from the charged Higgs, making this process sensitive to $\lambda_{3,7}$, $m_{H^\pm}$, and $\tilde{\alpha}$. The Higgs signal strength in the diphoton channel has been measured at the LHC, with the latest results from ATLAS [45] and CMS [46] being $\mu_{\gamma\gamma}^h = 1.17^{+0.28}_{-0.26}$ and $\mu_{\gamma\gamma}^h = 1.12 \pm 0.24$, respectively. The Higgs production cross section being the same as in the SM, the signal strength in the A2HDM reads [32,36]

$$\mu_{\gamma\gamma}^h = \frac{\sigma(pp \to h) \times \text{Br}(h \to 2\gamma)}{\sigma(pp \to h)_{\rm SM} \times \text{Br}(h \to 2\gamma)_{\rm SM}} \simeq (1 - 0.15C_{H^\pm}^h)^2, \quad \text{with} \tag{13}$$

$$C_{H^\pm}^h = \frac{v^2}{2m_{H^\pm}^2} x_{H^\pm}\lambda_{H^+H^-}^h\left(-1 + x_{H^\pm}\arcsin^2\left(\frac{1}{\sqrt{x_{H^\pm}}}\right)\right), \tag{14}$$

where $x_{H^\pm} = 4m_{H^\pm}^2/m_h^2$. We have imposed the condition that $\mu_{\gamma\gamma}^h$ in our case should lie within the 2σ range of the experimental measurements. Additionally, the $\lambda_{H^+H^-}^h$

coupling ($\simeq\lambda_3\cos\tilde{\alpha}+\lambda_7\sin\tilde{\alpha}$) in Eq. (14) is required to be less than 4π to ensure the validity of perturbation theory. However, for a light charged Higgs, this cubic coupling receives a sizable one-loop scalar contribution [32],

$$(\lambda^h_{H^+H^-})_{\rm eff}=\lambda^h_{H^+H^-}(1+\Delta),\quad \text{with}$$
$$\Delta=\frac{v^2(\lambda^h_{H^+H^-})^2}{16\pi^2 m^2_{H^\pm}}\mathcal{Z}\left(\frac{m^2_h}{m^2_{H^\pm}}\right), \tag{15}$$

with

$$\mathcal{Z}(X)=\int_0^1 dy\int_0^{1-y} dz[(y+z)^2+X(1-y-z-yz)]^{-1}. \tag{16}$$

Since a large correction to $\lambda^h_{H^+H^-}$ could invalidate the perturbation theory, at most 50% corrections are allowed, i.e., $\Delta\leq 0.5$. The other theoretical bounds considered are the perturbativity bounds on the quartic scalar couplings $|\lambda_{2,3,7}|<4\pi$, the requirement of the stability of the scalar potential [2], and the unitarity of the S-wave scattering amplitudes of the scalars [47].[2] Additionally, the electroweak precision tests provide important constraints on the parameters of the A2HDM. The mass splittings between the additional scalars of the A2HDM are constrained by the S, T, and U parameters [51]. It was shown in Ref. [36] that in order to satisfy the precision electroweak constraints the mass differences $|m_{H^\pm}-m_H|$ and $|m_{H^\pm}-m_A|$ cannot both be larger than v at the same time. Taking into account all these constraints, we perform a scan in the m_A, m_H, $m_{H^\pm}$, $\lambda_{2,3,7}$ parameter space. The points for the scan are generated in the intervals

$$\lambda_2\in(0,4\pi),\qquad \lambda_3\in(-4\pi,4\pi),\qquad \lambda_7\in(-4\pi,4\pi),$$
$$m_{H^\pm}\in(180\ \text{GeV},1\ \text{TeV}),$$
$$m_H\in(180\ \text{GeV},1\ \text{TeV}),\qquad m_A\in(180\ \text{GeV},1\ \text{TeV}). \tag{17}$$

The allowed parameter space for the scalar mass differences $m_{H^\pm}-m_A$ and $m_{H^\pm}-m_H$ is shown in Fig. 1. This shows that there can be three possible scenarios:

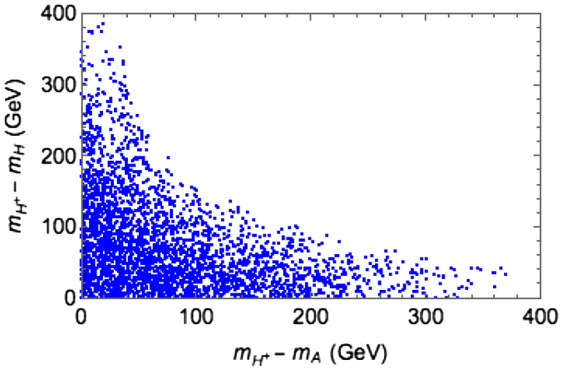

FIG. 1. The region of scalar mass splitting in the $|m_{H^\pm}-m_H|$ vs the $|m_{H^\pm}-m_A|$ plane, allowed by the Higgs signal strength in the diphoton channel, perturbativity bounds on the quartic scalar couplings $|\lambda_{2,3,7}|<4\pi$, stability of scalar potential, unitarity of S-wave scattering amplitudes, and electroweak precision data.

(i) *Case 1:* $|m_{H^\pm}-m_A|\geq 200$ GeV and $|m_{H^\pm}-m_H|\leq 40$ GeV.
(ii) *Case 2:* $|m_{H^\pm}-m_H|\geq 200$ GeV and $|m_{H^\pm}-m_A|\leq 40$ GeV.
(iii) *Case 3:* $|m_{H^\pm}-m_H|\simeq|m_{H^\pm}-m_A|\leq 40$ GeV.

We will later discuss the decay width of $H^\pm\to W^\pm Z$ in the context of these three scenarios. After discussing the constraints on the couplings and the physical masses, we will now study the constraints on the alignment parameters in the next sections.

A. Impact on $\varsigma_{u,d,\ell}$ from flavor observables and direct LHC searches of charged Higgs

First, we discuss the constraints currently available on the alignment parameters from flavor physics. The inclusive $B\to X_{s,d}\gamma$ branching ratio constrains the $\varsigma_u-\varsigma_d$ parameter space. The alignment parameter for the up quark is additionally constrained from the $B^0_{s,d}-\bar{B}^0_{s,d}$ mixing and from the $Z\to b\bar{b}$ decay width. The $Z\to b\bar{b}$ branching ratio leads to a linear dependence on the charged Higgs mass, which implies [23]

$$|\varsigma_u|<0.72+0.0024\ m_{H^\pm}\text{GeV}^{-1},\quad (\text{at } 95\%\ \text{CL}). \tag{18}$$

The other two alignment parameters $\varsigma_{d,\ell}$ are constrained with the requirement that the Yukawa couplings should remain within the perturbative regime, $(\sqrt{2}\varsigma_{d,\ell}m_{d,\ell}/v<1)$, leading to absolute upper bounds $|\varsigma_d|<50$ and $|\varsigma_\ell|<100$. For our analysis, we vary the alignment parameters in the following region, taking into account the above constraints as well as the flavor constraints from radiative inclusive $B\to X_{s,d}\gamma$ decays [23],

$$\varsigma_u\in(-3,3),\qquad \varsigma_d\in(-50,50),\qquad \varsigma_\ell\in(-100,100). \tag{19}$$

[2]The one-loop corrections affect the stability of the electroweak potential in the presence of large scalar couplings. It was shown in Ref. [48] that for most values of λ_i's where the scalar potential is stable at tree level the stability is also maintained at one loop. The authors also showed that for many values of λ_i, which are excluded by the tree-level stable vacuum conditions, inclusion of one-loop corrections revives them. We ignore the one-loop corrections in our work for simplicity, as we expect including them will result in a small increase in the allowed parameter space with little effects on our results and conclusions. Recently, in Refs. [49,50], it was demonstrated that the unitarity bounds on the quartic scalar couplings gets improved for a finite s in models with additional scalars coupling to the Higgs. These issues are interesting but beyond the scope of this work.

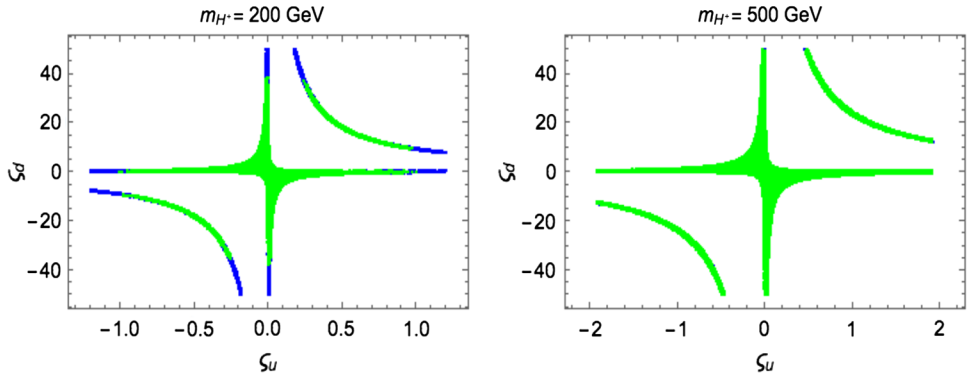

FIG. 2. The regions in the $\varsigma_u - \varsigma_d$ plane that are allowed by flavor physics data (blue points) and constraints from the tb decay channel of the charged Higgs where $H^\pm$ is produced in association with a top quark at the 13 TeV LHC (green points). The regions are shown for two choices of the charged Higgs mass $m_{H^\pm} = 200$ and 500 GeV.

Apart from the bounds considered before, the direct searches of new scalars at the LHC and LEP provide additional constraints on the model parameters. Here, we will consider the constraints coming from the charged Higgs searches. The LEP collaborations searched for a charged Higgs in the $e^+e^- \to H^+H^-$ channel with the charged Higgses reconstructed from $H^+ \to c\bar{s}$ and $\tau^+\nu_\tau$. The nonobservation of any signal at the LEP collaboration puts a lower bound on the charged Higgs mass: $m_{H^\pm} \geq 78.6$ GeV [52] at 95% CL in the 2HDM of type II.

The LHC has searched for a light charged Higgs in the $t \to H^\pm b$ channel and has excluded $m_{H^\pm} \in (80, 160)$ GeV [53]. The LHC Collaboration has also looked for a heavy charged Higgs in the $pp \to t(b)H^\pm$ process with $H^\pm \to \tau^\pm\nu_\tau$ [53,54], $H^\pm \to tb$ [55], and $H^\pm \to W^\mp Z$ [56] and has given a model-independent limit on $\sigma(pp \to t(b)H^\pm) \times \mathrm{BR}(H^\pm \to \tau^\pm\nu_\tau, tb)$ as a function of $m_H^\pm$. We use this limit to constrain the alignment parameters, in addition to the constraints from flavor observables discussed above.

To implement the LHC bounds, we calculate the process $\sigma(pp \to t(b)H^\pm) \times \mathrm{BR}(H^\pm \to \tau^\pm\nu_\tau, tb)$ in the A2HDM in MADGRAPH [57]. The dependence of the alignment parameters on the production cross section $\sigma(pp \to t(b)H^\pm)$ comes through the vertex $\lambda_{tb}^{H^\pm} = \varsigma_u m_t P_L - \varsigma_d m_b P_R$. The decay widths of the charged Higgs to tb and $\tau\nu_\tau$ are also sensitive to the alignment parameter and are given by

$$\begin{aligned}\Gamma(H^\pm \to tb) = &\frac{3\lambda^{1/2}(m_{H^\pm}^2, m_t^2, m_b^2)}{8\pi v^2 m_{H^\pm}^3} \\ &\times [(m_{H^\pm}^2 - m_t^2)(m_b^2\varsigma_d^2 + m_t^2\varsigma_u^2) \\ &- m_b^2(m_b^2\varsigma_d^2 + m_t^2\varsigma_u^2) + 4m_b^2 m_t^2 \varsigma_d\varsigma_u] \\ \Gamma(H^\pm \to \tau^\pm\nu_\tau) = &\frac{m_\tau^2\varsigma_\ell^2}{8\pi v^2 m_{H^\pm}^3}[m_{H^\pm}^2 - m_\tau^2]^2, \end{aligned} \tag{20}$$

with $\lambda(a,b,c) = (a-b-c)^2 - 4bc$.

In our numerical analysis, we have also added the branching ratios into cs, ud, and $\mu\nu_\mu$, which can be trivially obtained from the above formulas. In the limit $m_{H^\pm} > m_W + m_{\varphi_i}$, where $\varphi_i = h, H, A$, the decay $H^\pm \to W^\pm\varphi_i$ is kinematically allowed. The corresponding decay width is given by

$$\Gamma(H^\pm \to W^\pm\varphi_i) = \frac{\lambda^{3/2}(m_{H^\pm}^2, m_W^2, m_{\varphi_i}^2)}{16\pi v^2 m_{H^\pm}^3} R_i^2, \tag{21}$$

with $R_{h(H)} = \sin(\cos)\tilde{\alpha}$ and $R_A = 1$.

Compared to the other fermionic modes, $H^\pm \to tb$ has the dominant branching ratio for sizable alignment parameters since it depends on the mass of the top quark. Therefore, the tb decay channel at the LHC can be used to further constrain the $\varsigma_u - \varsigma_d$ parameter space. The decay width $\Gamma(H^\pm \to W^\pm\varphi_i)$ being independent of the alignment parameters, when kinematically allowed, the $\mathrm{BR}(H^\pm \to W^\pm\varphi_i)$ will be dominant in the limit of small values of alignment parameters. Note that, since $|\varsigma_\ell| < 100$ [24,42] is a very weak constraint, the $\mathrm{BR}(H^\pm \to \tau^\pm\nu_\tau)$ could dominate for a light charged Higgs.

Following these discussions, we now present in Figs. 2 and 3 the constraints on the $\varsigma_u - \varsigma_d$ and $\varsigma_u - \varsigma_\ell$ parameter space from the LHC process $\sigma(pp \to t(b)H^\pm) \times \mathrm{BR}(H^\pm \to \tau^\pm\nu_\tau, tb)$. To obtain the bounds, we simply demand that the theoretical value of the quantity $\sigma(pp \to t(b)H^\pm) \times \mathrm{BR}(H^\pm \to \tau^\pm\nu_\tau, tb)$ is smaller than the LHC limit. For simplicity, the results are shown for two choices of the charged Higgs mass, 200 and 500 GeV, and unless otherwise mentioned, this choice will be used in the numerical analyses presented in this work. The blue region is the one allowed by the flavor observables, whereas the region allowed when including the LHC information is shown in green. Overall, the green region is allowed by both the LHC and the flavor physics constraints. It can be seen from the left plot of Figs. 2 and 3 that only for low charged Higgs masses ($m_{H^\pm} < 500$ GeV) is the LHC search currently sensitive to the alignment parameter space allowed by flavor physics. The allowed range of the aligned

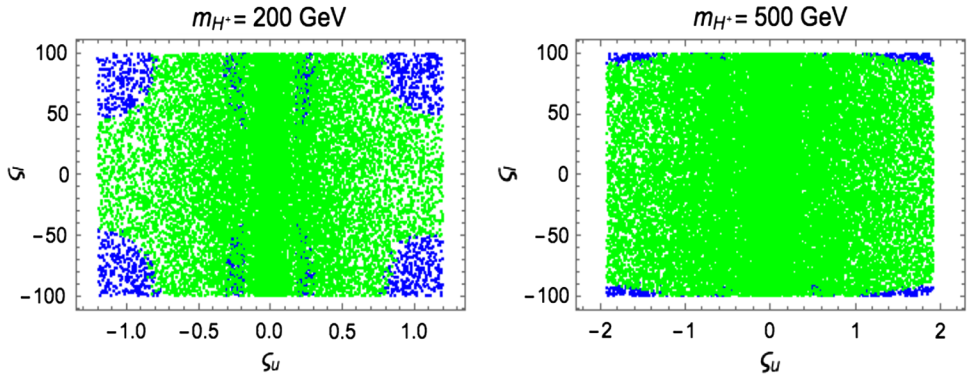

FIG. 3. The regions in the $\varsigma_u - \varsigma_\ell$ plane that are allowed by flavor physics data (blue points) and constraints from the $\tau\nu_\tau$ decay channel of the charged Higgs where $H^\pm$ is produced in association with a top quark at the 13 TeV LHC (green points). The regions are shown for two choices of the charged Higgs mass $m_{H^\pm} = 200$ and 500 GeV.

parameter ς_d for $m_{H^+} = 200$ GeV lies between approximately -40 and $+40$, and of the parameter ς_l is between approximately -50 and $+50$ as can be observed from Figs. 2 and 3.

IV. $H^\pm \to W^\pm Z$ DECAY IN THE A2HDM

In this section, we compute the $H^\pm W^\mp Z$ vertex at one loop in the A2HDM. We have performed the calculations analytically, and to reduce any risk of errors, our computations are tested by specific one-loop open source packages. The FeynCalc package [58,59] is used in the analytical computations. The packages that are being used to test our analytical results are the publicly available FeynRules [60] model files for 2HDM in which we have implemented the A2HDM. We generate the FeynArts [61] model files in FeynRules, and the amplitudes are calculated using FormCalc [62]. We have also compared our results numerically using LoopTools [62]. The diagrams are calculated here in the 't Hooft-Feynman gauge.

The loop contributions of the scalars/bosons to the $H^\pm W^\mp Z$ vertex are shown in Figs. 4 and 5, and the contributions of fermion loops are shown in Fig. 6. We have parametrized the $H^\pm \to W^\pm Z$ amplitude as

$$\mathcal{M} = g m_W \mathcal{M}_{\mu\nu} \epsilon_W^{\mu *} \epsilon_Z^{\nu *}, \quad \text{with}$$
$$\mathcal{M}_{\mu\nu} = \mathcal{F} g_{\mu\nu} + \frac{\mathcal{G}}{m_W^2} p_{Z\mu} p_{W\nu} + \frac{\mathcal{H}}{m_W^2} \epsilon_{\mu\nu\rho\sigma} p_Z^\rho p_W^\sigma, \tag{22}$$

where $\epsilon^\mu_{W,Z}$ are the polarizations of the gauge bosons and $p_{W,Z}$ are the momenta. The decay width for $H^\pm \to W^\pm Z$ in terms of the form factors $\mathcal{F}$, $\mathcal{G}$, and $\mathcal{H}$ listed in Eq. (22) is given as

$$\Gamma(H^+ \to W^+ Z) = m_{H^\pm} \frac{\lambda^{1/2}(1, w, z)}{16\pi} (|\mathcal{M}_{LL}|^2 + |\mathcal{M}_{TT}|^2), \tag{23}$$

where $w = m_W^2/m_{H^\pm}^2$, $z = m_Z^2/m_{H^\pm}^2$ and $\lambda(a, b, c) = (a - b - c)^2 - 4bc$. The amplitudes $\mathcal{M}_{LL}$ and $\mathcal{M}_{TT}$ contain the contributions from the longitudinally and transversely polarized gauge bosons and are given by

$$|\mathcal{M}_{LL}|^2 = \frac{g^2}{4z} \left| (1 - w - z)\mathcal{F} + \frac{\lambda(1, w, z)}{2w} \mathcal{G} \right|^2 \tag{24}$$

$$|\mathcal{M}_{TT}|^2 = g^2 \left(2w|\mathcal{F}|^2 + \frac{\lambda(1, w, z)}{2w} |\mathcal{H}|^2 \right), \quad \text{with}$$
$$\mathcal{F} = \frac{1}{g m_W} F, \qquad \mathcal{G} = \frac{m_W}{g} G, \qquad \mathcal{H} = \frac{m_W}{g} H. \tag{25}$$

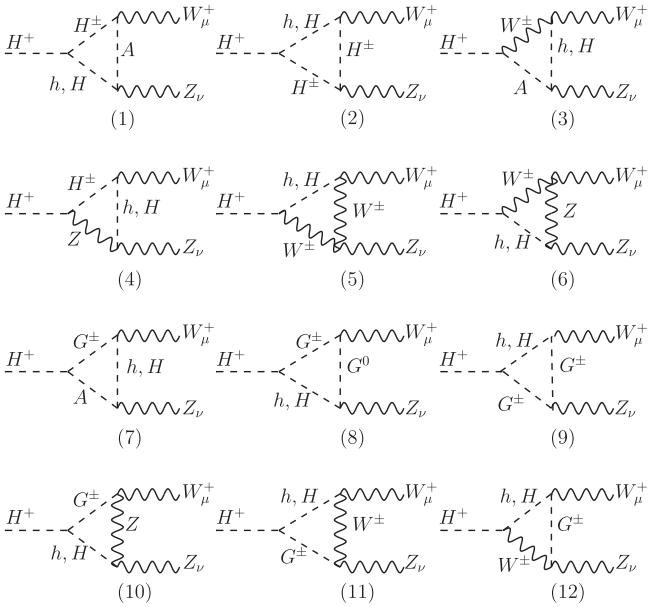

FIG. 4. The boson-loop triangle diagrams for $H^+ \to W^+ Z$ in the 't Hooft-Feynman gauge.

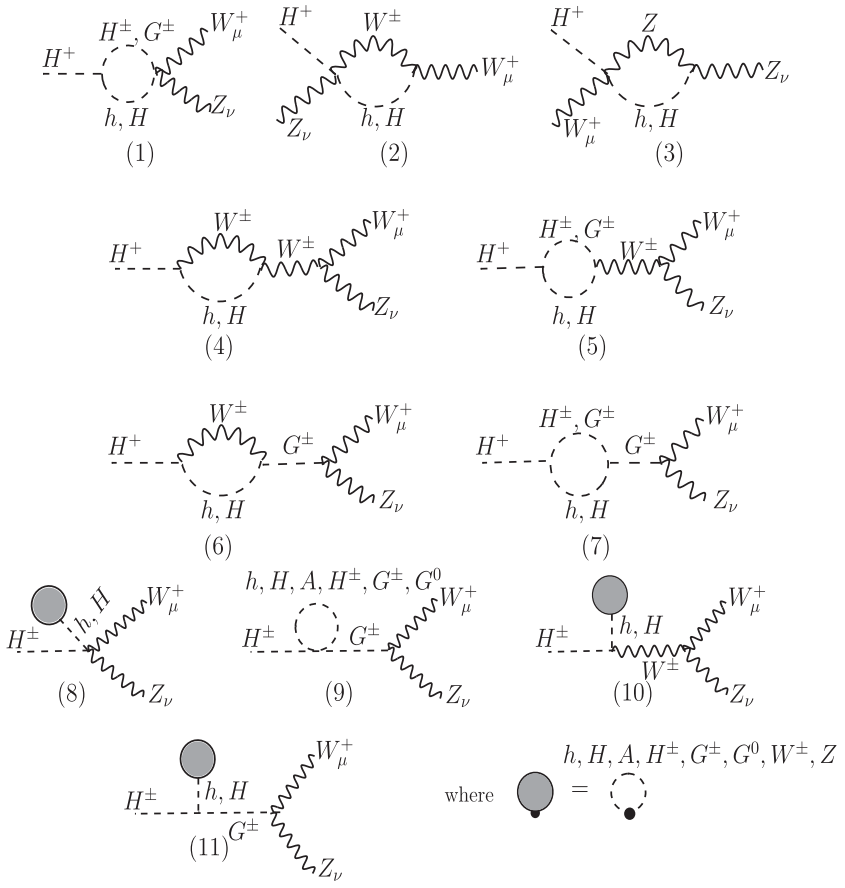

FIG. 5. The boson-loop and tadpole diagrams for $H^+ \to W^+Z$ in the 't Hooft-Feynman gauge.

The contributions to F, G, and H from individual diagrams in Figs. 4–6 are listed in Tables II–IV of Appendix A. The $\mathcal{F}$ term receives contributions from all the diagrams of Figs. 4, 5, and 6, whereas $\mathcal{G}$ only receives contributions from the boson and fermion triangle diagrams. The fermion-loop triangle diagrams only contribute to $\mathcal{H}$ as the boson sector in our case has the parity symmetry.

The dominant contributions to the $H^\pm W^\mp Z$ vertex come from the top quark mass as well as from the nondecoupling effects of the masses of the heavy scalars running in the loop. In the context of the type-II 2HDM, it was discussed in Ref. [15] that, with the $H^\pm tb$ coupling being proportional to $m_t \cot\beta$ and $m_b \tan\beta$, the fermion-loop contributions rapidly decrease for larger $\tan\beta$. The decrease of the fermion-loop contributions in the case of large $\tan\beta$ is compensated by the scalar nondecoupling effects, with a large mass splitting between m_A and $m_{H^\pm}$. Overall, the decay width in the 2HDM is proportional to the top quark contribution in the low $\tan\beta$ region and to the scalar nondecoupling effects in the large $\tan\beta$ region.

In the A2HDM, the dominant fermionic contributions to the $H^\pm W^\mp Z$ vertex are proportional to $m_t\varsigma_u$, $m_b\varsigma_d$, and

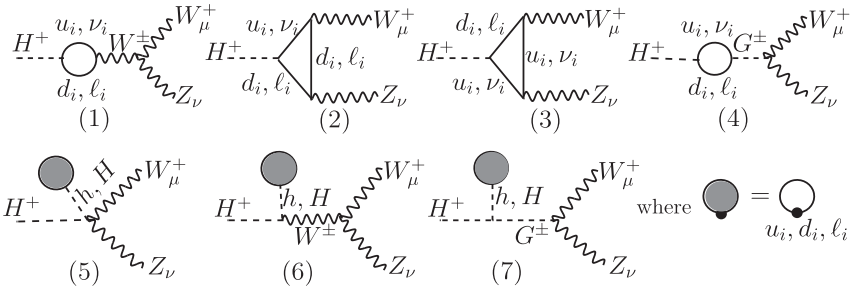

FIG. 6. The fermion-loop diagrams for $H^+ \to W^+Z$ in the 't Hooft-Feynman gauge. Note that i in u_i, d_i, ℓ_i, and ν_i stands for the fermion generation.

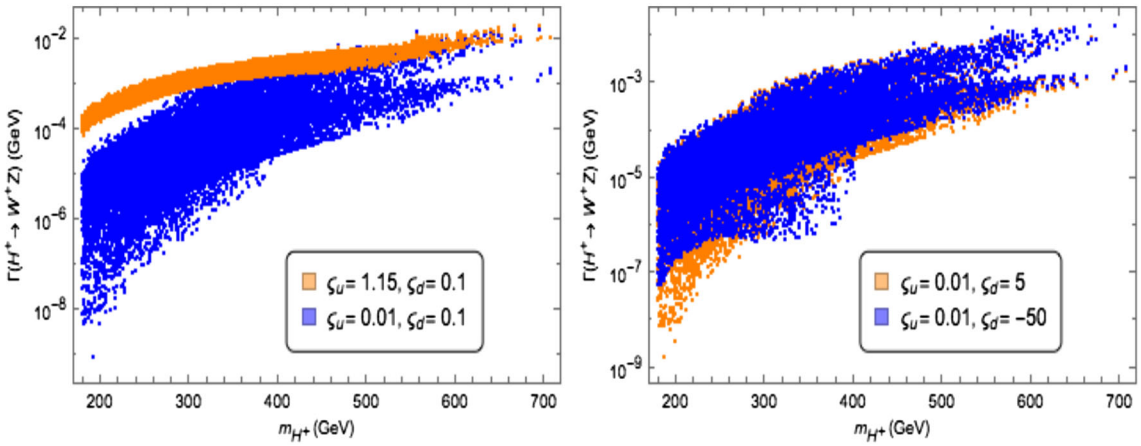

FIG. 7. The decay width $\Gamma(H^+ \to W^+Z)$ as a function of m_H^+ for various values of ς_u and ς_d with $\cos\tilde{\alpha} = 0.95$, $|m_{H^\pm} - m_A| > 200$ GeV and $m_H = m_{H^\pm} \pm 15$ GeV. The couplings $\lambda_{3,7,8}$ take the values allowed by the theoretical constraints, whereas the alignment parameter $\varsigma_\ell = 50$.

$m_\tau \varsigma_\ell$. Hence, for sufficiently large ς_u, the magnitude of the $H^\pm W^\mp Z$ vertex could be enhanced even for small values of the aligned parameter ς_d. This is starkly different from the results in the 2HDM of type II. The boson-loop contributions to the $H^\pm W^\mp Z$ vertex are mainly dependent on the splitting of the charged and pseudoscalar Higgs masses and the three independent parameters of the scalar potential $\lambda_{2,3,7}$.

Since there are too many free parameters involved, we will show our results for some particular benchmark values. Our results do not deviate drastically if we change these benchmark values. We first explore the dependence of the decay width on the charged Higgs mass and show in Fig. 7 the decay width as a function of $m_{H^\pm}$ for the mass splittings $|m_{H^\pm} - m_A| > 200$ GeV and $m_H = m_{H^\pm} \pm 15$ GeV. The couplings $\lambda_{2,3,7}$ are varied in the allowed range, satisfying the required experimental and theoretical constraints as discussed before. We have fixed the mixing angle value to $\cos\tilde{\alpha} = 0.95$, in accordance with the latest LHC results for all our calculations unless otherwise mentioned. The left plot shows the variation for two choices of $\varsigma_u = 0.01$ and 1.15, and ς_d is fixed to 0.1. In the plot to the right, we fix ς_u at 0.01, and ς_d is chosen 5 and -50. We have explicitly checked that the decay width does not change much with ς_ℓ; therefore, it is kept fixed at 50 for these plots. These figures show that the decay widths are quite sensitive to ς_u for a given charged Higgs mass.

We next consider the Higgs effect from the scalar-loop diagrams and show the dependence of the decay width on the Higgs mass splittings and the $\lambda_{2,3,7}$ parameters. The bosonic diagrams with the SM-like Higgs h in the loop are proportional to $\sin\tilde{\alpha}$ and therefore have a very small contribution. Therefore, a large value of the scalar self-coupling constant λ_7 (proportional to $\cos\tilde{\alpha}$ for the diagrams with H in the loop) is considered in order to make the contributions from the boson and fermion-loop diagrams comparable. The parameter λ_2 does not contribute to our process, whereas λ_3 is always accompanied with $\sin\tilde{\alpha}$ in most of the diagrams that contribute. We therefore work in the limit where the parameters $\lambda_{2,3}$ are fixed to zero and a large nonzero value for $\lambda_7 \simeq 8$ is considered.

We now show in Fig. 8 the ς_u dependence of the decay width for $m_{H^+} = 200$, 500 GeV with various mass splittings between the charged and the CP-odd scalars. The $\lambda_{2,3,7}$ parameters are fixed to values as discussed above, and ς_d is varied in the range $[-50,50]$. The decay width dependence on the different mass splitting scenarios can be easily interpreted from the figure. The case in which the additional scalars are degenerate (orange points) is sensitive to ς_u, as the contribution from scalar-loop diagrams gets suppressed with respect to the remaining contributions from the fermions and the gauge boson–loop diagrams. The top mass contribution to the decay width becomes very small in the limit where ς_u tends to zero. The blue points in Fig. 8 with a mass splitting $m_A - m_{H^+} = 200$ GeV show that the decay width is not small for small ς_u. This is because the top mass effect is dominant at large ς_u, whereas in the low ς_u region, the top mass contribution is decreased but the nondecoupling effects of heavier scalars increase the strength of the $H^\pm W^\mp Z$ vertex.

The reason for enhancement for the case in which the CP-odd scalar is degenerate with the charged Higgs while there is a large mass splitting between the heavy CP-even scalar and the charged Higgs (green points) is similar to the orange region; that is, large values of the aligned parameter ς_u and the mass of the top quark contribute through the fermionic loop. The results for the decay width shown in Fig. 8 are sensitive to λ_7, as the HH^+H^- vertex in the scalar-loop diagrams is proportional to λ_7. Therefore, with the decrease in the value of λ_7, the contribution from the fermionic loop diagrams becomes dominant, and the decay width becomes sensitive to ς_u, irrespective of the mass

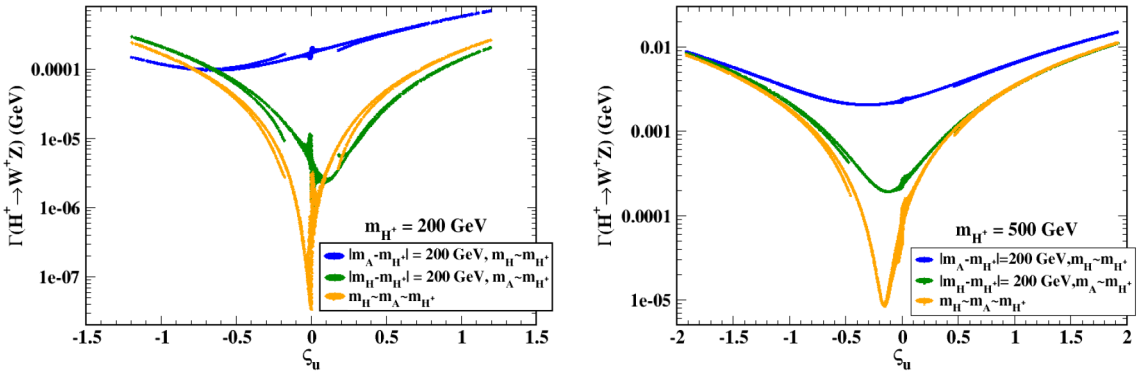

FIG. 8. Decay width $\Gamma(H^+ \to W^+Z)$ as a function of ς_u for different mass splittings between charged and CP-odd scalars with $\cos\tilde{\alpha} = 0.95$. The parameter ς_d is varied in the allowed range, whereas the other parameters are fixed as discussed in the text. The figures are shown for two choices of charged Higgs mass $m_{H^+} = 200$ and 500 GeV.

splitting between the scalars. The contribution from the scalar-loop diagrams is therefore dominant with a large mass splitting and large allowed values of $|\lambda_7|$, for $\cos\tilde{\alpha} = 0.95$.

The Higgs mass effect is dominant when the $m_A - m_{H^+}$ mass splitting is large. We discuss this scenario in details in the following. We plot the decay width as a function of m_A for different choices of ς_u in Fig. 9. The results remain the same with the variation of ς_d and ς_ℓ, which we fix at 0.1 and 50 in these figures. The other parameters are similar to those in the previous figure. We can see from Fig. 9 that the decay width becomes independent of ς_u for large mass splitting between m_A and m_{H^+}. In the near custodial symmetry limit ($m_A \simeq m_{H^+}$), the nondecoupling effects of the scalar masses are highly suppressed, and the decay width receives contribution only from the fermionic and the gauge boson diagrams, making the decay width sensitive to ς_u.

We now consider the branching ratio (BR) for the process $H^+ \to W^+Z$. The decay is kinematically allowed when the charged Higgs mass $m_{H^\pm} > m_W + m_Z$. The threshold of $H^\pm \to tb$ is also very close to $m_W + m_Z$. The tb mode becomes dominant for large values of $\varsigma_{u,d}$ when $m_{H^\pm} > m_t + m_b$. We note that for $m_{H^\pm}$ around 200 GeV only the decay mode $\tau\nu_\tau$ dominates over the W^+Z decay for large values of ς_ℓ. This can be seen from the first plot of Fig. 10 in which we show the branching ratio of the charged Higgs as a function of m_A. The $\tau\nu_\tau$ mode is shown with a green color, and the W^+Z mode is in blue. With $\varsigma_\ell = 50$, the leptonic decay channel has a branching ratio of almost 1, whereas the BR of W^+Z increases with the variation of $\varsigma_u = 0.01$ (solid) to $\varsigma_u = 1.15$ (dashed). It should be noted that the value of $\lambda_{2,3}$ are fixed at zero, $\lambda_7 \simeq$ at 8 and ς_d at 0.1. In the limit of vanishing ς_ℓ and $m_{H^\pm}$ around 200 GeV, the BR for W^+Z will be 1. For a heavy charged Higgs, various other decay channels open up, as

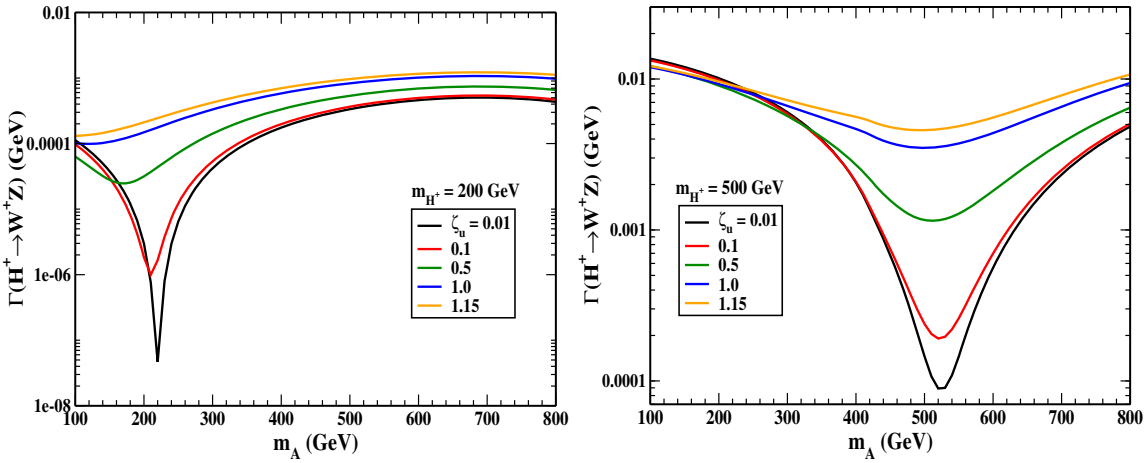

FIG. 9. The decay width $\Gamma(H^+ \to W^+Z)$ as a function of m_A for different values of the Yukawa alignment parameter ς_u with $\varsigma_d = 0.1$, $\varsigma_\ell = 50$, $\cos\tilde{\alpha} = 0.95$, $m_H = m_{H^+} + 10$ GeV, and $\lambda_{2,3} = 0$. The figures are shown for two values of charged Higgs mass $m_{H^+} = 200$, 500 GeV.

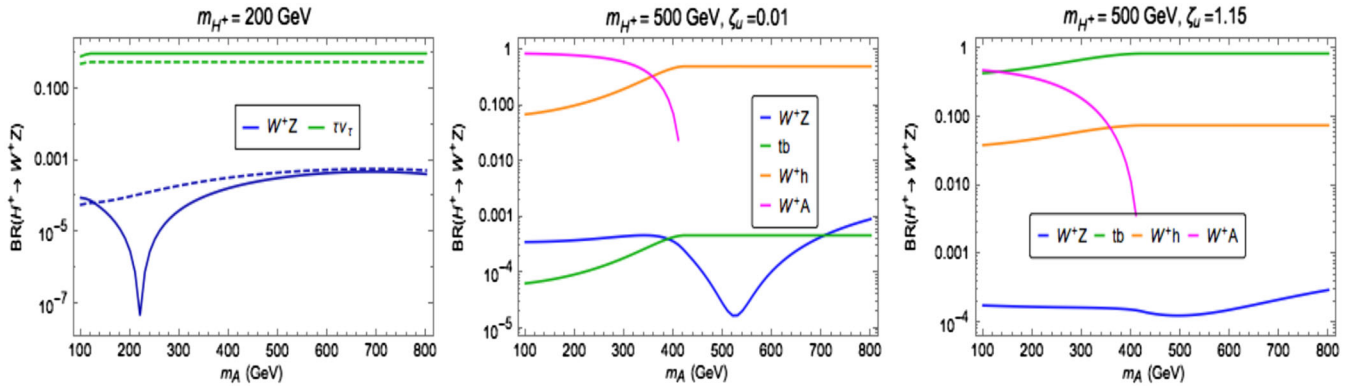

FIG. 10. The branching ratio $\Gamma(H^+ \to W^+Z)$ as a function of m_A for $\lambda_{2,3} = 0$, $\varsigma_d = 0.1$, $\varsigma_\ell = 50$, $m_H = m_{H^+} + 10$ GeV, and $\cos\tilde{\alpha} = 0.95$. The other dominant branching ratios of H^+ are also shown. In the left plot, the solid lines are for $\varsigma_u = 0.01$, and the dashed lines are for $\varsigma_u = 1.15$.

can be seen from the second and third plots of Fig. 10. The tb final state has a dominant branching ratio for large values of ς_u. The BR$(H^+ \to W^+Z))$ is larger than the one into tb when the alignment parameters are small for the region where there is a large mass difference between m_A and m_{H^+}, as seen from the second plot of Fig. 10. With smaller ς_u, a larger value of ς_d will lead to an enhanced branching ratio of tb, whereas the W^+Z will not be affected significantly.

Finally in Fig. 11, we show the branching ratio as a function of $m_{H^\pm}$ for two different scenarios. The left plot shows the branching ratio as a function of $m_{H^\pm}$ for the case in which $m_A \geq m_{H^\pm} \pm 200$ GeV and $m_H \approx m_{H^\pm} \pm 10$ GeV. In the right plot, we show the branching ratio for the case in which the CP-odd scalar and the CP-even heavy scalar are degenerate in mass ($m_A \approx m_H$). In these plots, $\lambda_{2,3,7}$ and the alignment parameters are all varied within the region allowed by the theoretical and experimental constraints. The branching ratio in the low mass range can be as large as 10^{-3}. A large branching ratio can be obtained for small alignment parameters, large λ_7, and a large mass difference $|m_A - m_{H^+}|$. The decay width increases with large ς_u, but this also leads to the enhancement of the dominant decay channel tb.

V. $H^\pm$ PRODUCTION THROUGH WZ FUSION AT THE LHC

In this section, we explore whether the BR$(H^\pm \to W^\pm Z)$ in the A2HDM could be large enough to be detected at the LHC. The charged Higgs for the mass range considered here will be mainly produced through the process $pp \to t[b]H^\pm$ with the dominant decay mode of $H^\pm$ being $H^\pm \to tb$, if kinematically allowed. The cross section for the $gb \to tH^\pm$ subprocess at the 13 TeV LHC with $\varsigma_u = 1.15$, $\varsigma_d = 0.1$ will be $\approx$4367 fb for $m_{H^\pm} = 200$ GeV and $\approx$454 fb for $m_{H^\pm} = 500$ GeV. This process has been studied at the LHC, and we have discussed the constraints on the

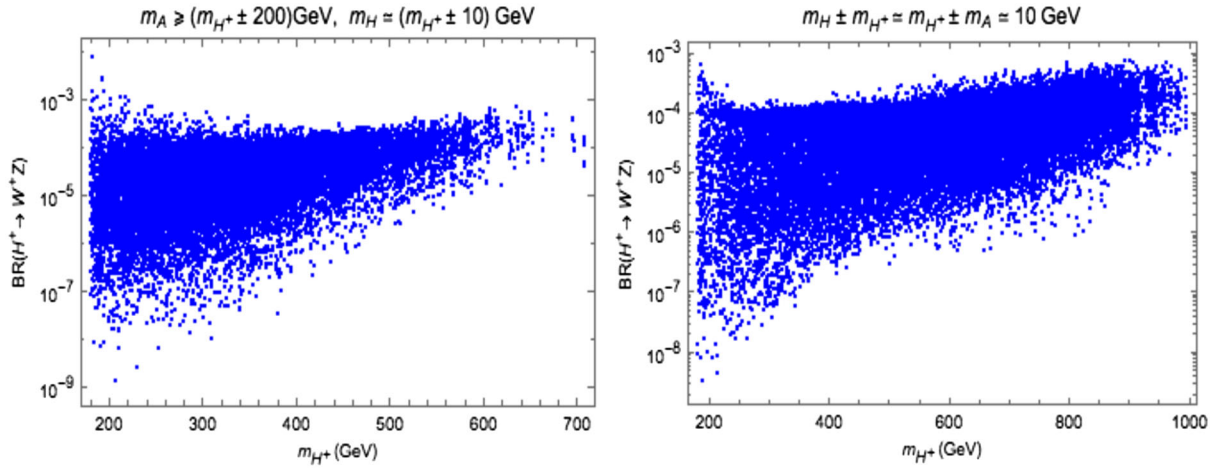

FIG. 11. The branching ratio BR$(H^+ \to W^+Z)$ as a function of m_H^+ for values of ς_u, ς_d, and ς_ℓ and the $\lambda_{3,7}$ parameters allowed by the theoretical and the experimental constraints discussed in the text.

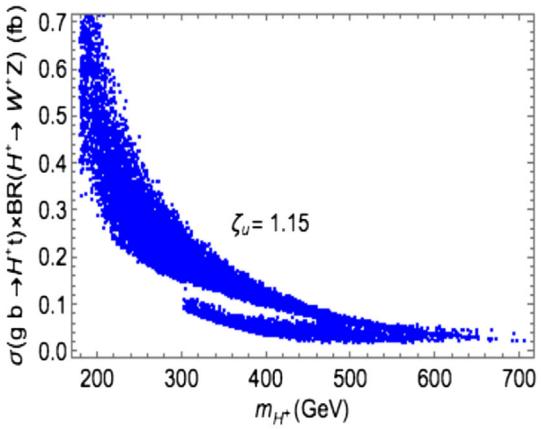

FIG. 12. The cross section of H^+ production in association with a top quark followed by its decay to W^+Z as a function of m_{H^+}.

alignment parameters from this process and the subsequent decay of the charged Higgs to tb, $\tau\nu_\tau$ in Sec. III A.

We show in Fig. 12 the expected cross section for the process $gb \to tH^+ \to tW^+Z$ at $\sqrt{s} = 13$ TeV as a function of $m_{H^\pm}$ with the couplings $\lambda_{2,3,7}$ varied in the allowed range. The alignment parameters are kept fixed as $\varsigma_u = 1.15$, $\varsigma_d = 0.1$, and we take $|m_A - m_{H^\pm}| = 200$ GeV, $|m_H - m_{H^\pm}| = 10$ GeV. The dominant SM background to this process will be $W^+Z + X$, which can be reduced with appropriate kinematic cuts on the final state. The signal in this final state can be observed at the high-luminosity LHC for low $m_{H^\pm}$ and $\varsigma_u \gtrsim 1$.

We next discuss the charged Higgs production through WZ fusion at the 13 TeV LHC and show in Fig. 13 the expected cross section assuming $\mathcal{G} = \mathcal{H} = 0$ for simplification. This is a good approximation as the loop induced $\mathcal{F}$ term is much larger than the $\mathcal{G}$ and $|\mathcal{H}|$ terms for most of the parameter space. We have calculated the production cross section of the charged Higgs through WZ fusion [63] in MADGRAPH. This process followed by the decay of the charged Higgs to WZ has been studied by the CMS Collaboration [56]. We present our results in Fig. 14,

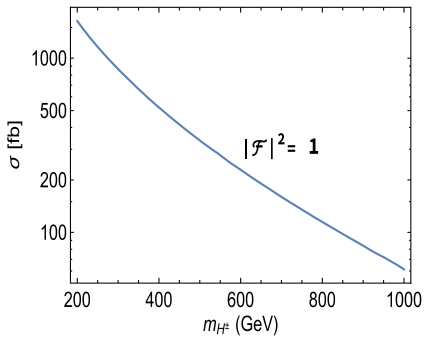

FIG. 13. The cross-section of H^+ production through WZ fusion at the 13 TeV LHC, with the form factor $\mathcal{F}$ set to unity and $\mathcal{G} = \mathcal{H} = 0$.

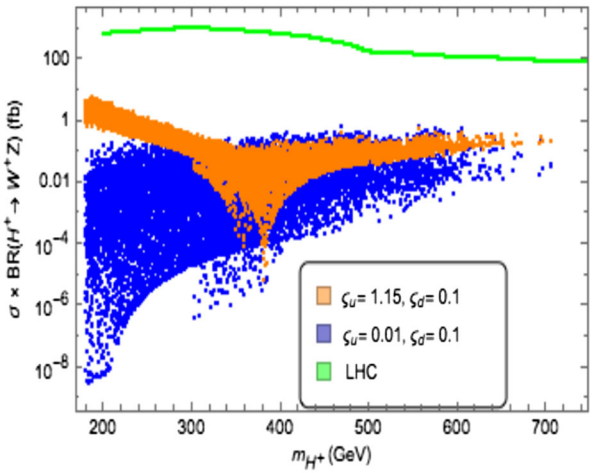

FIG. 14. σ for $H^\pm$ production through WZ fusion with subsequent decay of $H^\pm$ to $W^\pm Z$. The line in green is the current bound from LHC.

considering the parameter space where a large branching ratio of $H^\pm \to W^\pm Z$ is observed. The $\lambda_{2,3,7}$ parameters are varied, taking into account the theoretical and experimental constraints, and the mass differences between the additional Higgs boson are fixed at $|m_A - m_{H^\pm}| = 200$ GeV and $|m_H - m_{H^\pm}| = 10$ GeV. The green line is the current experimental bound from the LHC. At large $m_{H^\pm}$, we see that the cross section becomes comparable for $\varsigma_u = 0.01$ and 1.15. This is because the decay width of the tb decay channel is proportional to $\varsigma_u^2(m_{H^\pm}^2 - m_t^2)/m_{H^\pm}$ and for large $m_{H^\pm}$ will be $\sim\varsigma_u^2 m_{H^\pm}$. Therefore, at large $m_{H^\pm}$, the branching ratio of $W^\pm Z$ decreases with large ς_u.

We observe in Fig. 13 that the cross section can be as low as 1 fb as the mass of the charged Higgs goes beyond 1 TeV. Hence, when the luminosity of the LHC will be 300 fb^{-1}, 300 events with a charged Higgs can be produced for a 1 fb cross section. A similar conclusion can be drawn from Fig. 14 for the high-luminosity phase of the LHC. Thus, we see that the $H^\pm \to W^\pm Z$ in the A2HDM is within the reach of the high-luminosity phase of the LHC [64–66]. On the other hand, the $tH^\pm$ production channel will be dominant to produce a sufficient number of charged Higgs only in the lower mass region as can be seen from Fig 12 for a luminosity of 300 fb^{-1}. However, as the high-luminosity phase will move forward, this conclusion about the $tH^\pm$ production channel will not hold.

VI. SUMMARY

The custodial symmetry of the SM could have interesting implications if there exists an extended scalar sector. This may give rise to remarkable signatures such as an enhancement of the $H^\pm W^\pm Z$ vertex. This vertex is absent at tree level in the 2HDM because of the weak isospin symmetry of the kinetic terms of the Higgs sector and appears at one

loop. Furthermore, this vertex was studied in the 2HDM of type II before the discovery of the SM-like Higgs at the LHC [15,16].

In this work, we have investigated the $H^{\pm}W^{\pm}Z$ vertex using the 't Hooft Feynman gauge in the A2HDM. The computation was performed taking into account the theoretical constraints such as the vacuum stability, perturbative unitarity, and the bounds from the electroweak precision data. The experimental bounds from flavor physics observables as well as the direct searches of $H^{\pm}$ at the LHC are also taken into account. The latest results from the charged Higgs searches at the LHC are used to constrain the alignment parameters, as the production and decay mode of the charged Higgs are proportional to them. We find that for $m_{H^+} < 500$ GeV the LHC data from charged Higgs searches constrain the aligned parameters $\varsigma_{u,d,\ell}$ allowed by the flavor observables. The parameter space for $m_{H^{\pm}} \geq 500$ GeV is currently not sensitive to the LHC results.

We later discuss the nondecoupling effects of heavy scalars and fermions in the decay width of $H^+ \to W^+Z$ and find that the decay width is more sensitive to $m_t\varsigma_u$ compared to $m_{d,\ell}\varsigma_{d,\ell}$. We note that in the A2HDM for $\cos\tilde{\alpha}$ tending to 1, the nondecoupling effects from the boson-loop diagrams are proportional to λ_7 and a large mass splitting between the CP-odd Higgs and the charged Higgs. Hence, large values of the quartic coupling λ_7 helps enhance the magnitude of the $H^{\pm}W^{\pm}Z$ vertex. An enhancement of this vertex also occurs when the alignment parameter ς_u is large even if the alignment parameter ς_d is small.

The dependence of the decay width on each of the independent parameters is discussed individually. We have worked for the charged Higgs in the mass range 200–1000 GeV and found that the maximum obtainable branching ratio for the process considered here in light of the recent experimental constraints is around $\mathcal{O}(10^{-3})$.

Finally, we also calculate the two charged Higgs production modes at the LHC and its subsequent decay to W^+Z. The production modes are (1) H^+ produced in association with a top quark (2) H^+ produced singly through WZ fusion. The $W^{\pm}Z$ final state produced through WZ fusion in the A2HDM is within the reach of the future high-luminosity phase of the LHC.

ACKNOWLEDGMENTS

We are extremely grateful to Antonio Pich and Saurabh D. Rindani for reading the manuscript thoroughly, very useful discussions, comments, and suggestions on the manuscript. D. D. is supported by the DST, Government of India, under the INSPIRE Faculty Award (Grant No. DST/INSPIRE/04/2016/002620). M. P. acknowledges support of the Slovenian Research Agency through research core funding Grant No. P1-0035.

APPENDIX A: AMPLITUDES FOR $H^{\pm} \to W^{\pm}Z$ FOR FEYNMAN DIAGRAMS GIVEN IN DIAGRAMS FIGS. 4, 5, AND 6

We present in this section the F, G, and H form factors used to parametrize the one-loop decay amplitude defined in Eq. (22). We would like to point out that the fermion-loop contribution to the H^+W^-Z vertex was calculated earlier in the unitary gauge [15]. The fermion-loop diagrams by themselves form a gauge-invariant subset, whereas the boson-loop diagrams form another subset so that they can be independently calculated in an arbitrary gauge. We perform the calculation for the contributions from the boson and the fermion-loop diagrams in the 't Hooft-Feynman gauge and have explicitly checked that our results are finite. The F, G, and H terms are listed in Tables II, III, and IV. Here, we show the contributions to F, G, and H separately for each diagram. The notation is as follows: $F^{4[1]}$ indicates the contribution of the first diagram in Fig. 4, and so on. The same definition holds for the others. We list the various couplings used for the computation,

$$
\begin{aligned}
\lambda^{\varphi_i^0}_{H^{\pm}H^{\mp}} &= \lambda_3 R_{i1} + \lambda_7 R_{i2},\\
\lambda^{\varphi_i^0}_{AZ} &= \lambda^{\varphi_i^0}_{H^{\pm}W^{\mp}} = \lambda^{\varphi_i^0}_{H^{\pm}W^{\mp}Z} = R_{i2},\\
\lambda^{\varphi_i^0}_{W^{\pm}W^{\mp}} &= \lambda^{\varphi_i^0}_{ZZ} = \lambda^{\varphi_i^0}_{G^{\pm}W^{\mp}} = \lambda^{\varphi_i^0}_{G^0Z} = \lambda^{\varphi_i^0}_{G^{\pm}W^{\mp}Z} = R_{i1},\\
\lambda^{\varphi_i^0}_{G^{\pm}H^{\mp}} &= \lambda_6 R_{i1} + \left(\frac{\lambda_4}{2} + \lambda_5\right) R_{i2},\\
\lambda^{\varphi_i^0}_{G^{\pm}G^{\mp}} &= \lambda^{\varphi_i^0}_{G^0G^0} = 2\lambda_1 R_{i1} + \lambda_6 R_{i2},\\
\lambda^{\varphi_i^0}_{AA} &= (\lambda_3 + \lambda_4 - 2\lambda_5) R_{i1} + \lambda_7 R_{i2},\\
\lambda^{\varphi_i^0}_{\varphi_i^0\varphi_i^0} &= 2\lambda_1 R_{i1}^3 + R_{i2}^2 R_{i1}(\lambda_3 + \lambda_4 + 2\lambda_5)\\
&\quad + 3\lambda_6 R_{i2} R_{i1}^2 + \lambda_7 R_{i2}^3\\
\lambda^{\varphi_i^0}_{\varphi_j^0\varphi_j^0} &= 6\lambda_1(-R_{i1}^3 + R_{i1} + 3R_{i1}R_{i2}^2)\\
&\quad + (\lambda_3 + \lambda_4)(3R_{i1}^3 + R_{i1} - 9R_{i2}^2 R_{i1})\\
&\quad + 2\lambda_5(3R_{i1}^3 + R_{i1} - 9R_{i1}R_{i2}^2)\\
&\quad + 3\lambda_6(3R_{i2}^3 + R_{i2} - 9R_{i1}^2 R_{i2})\\
&\quad + 3\lambda_7(-R_{i2}^3 + R_{i2} + 3R_{i1}^2 R_{i2}) \quad \text{for } i \neq j,\\
\lambda^{\varphi_i^0}_{f\bar{f}} &= R_{i1} + \varsigma_f R_{i2},
\end{aligned}
\tag{A1}
$$

where R_{ij} denotes the ij element of the orthogonal R matrix, which determines the neutral CP-even Higgs boson mass eigenstates defined in Eq. (5).

APPENDIX B: LOOP INTEGRALS

We have used the dimensional regularization scheme for our calculation, with the approach similar to one given in

TABLE II. The F and G terms from the boson triangle loop diagrams in Fig. 4 contributing to the decay $H^+ \to W^+Z$, with $\varphi_1^0 = h$ and $\varphi_2^0 = H$.

Fig. 4	Amplitude	Argument
$F^{4[1]}$	$-\frac{g^2 v}{c_W}\lambda^{\varphi_i^0}_{H^+H^-}\lambda^{\varphi_i^0}_{AZ}C_{24}$	$[p_W, -p_{H^\pm}, m_A, m_{H^\pm}, m_{\varphi_i^0}]$
$G^{4[1]}$	$-\frac{g^2 v}{c_W}\lambda^{\varphi_i^0}_{H^+H^-}\lambda^{\varphi_i^0}_{AZ}(C_{22}-C_{23})$	$[p_W, -p_{H^\pm}, m_A, m_{H^\pm}, m_{\varphi_i^0}]$
$F^{4[2]}$	$\frac{g^2 v}{c_W}(c_W^2-s_W^2)\lambda^{\varphi_i^0}_{H^+H^-}\lambda^{\varphi_i^0}_{W^\pm H^\mp}C_{24}$	$[p_W, -p_{H^\pm}, m_{H^\pm}, m_{\varphi_i^0}, m_{H^\pm}]$
$G^{4[2]}$	$\frac{g^2 v}{c_W}(c_W^2-s_W^2)\lambda^{\varphi_i^0}_{H^+H^-}\lambda^{\varphi_i^0}_{W^\pm H^\mp}(C_{22}-C_{23})$	$[p_W, -p_{H^\pm}, m_{H^\pm}, m_{\varphi_i^0}, m_{H^\pm}]$
$F^{4[3]}$	$-\frac{g^4 v}{4c_W}\lambda^{\varphi_i^0}_{AZ}\lambda^{\varphi_i^0}_{W^\pm W^\mp}C_{24}$	$[p_W, -p_{H^\pm}, m_{\varphi_i^0}, m_{W^\pm}, m_A]$
$G^{4[3]}$	$-\frac{g^4 v}{4c_W}\lambda^{\varphi_i^0}_{AZ}\lambda^{\varphi_i^0}_{W^\pm W^\mp}(2(C_{12}-C_{11})+C_{22}-C_{23})$	$[p_W, -p_{H^\pm}, m_{\varphi_i^0}, m_{W^\pm}, m_A]$
$F^{4[4]}$	$\frac{g^4 v}{4c_W^3}(c_W^2-s_W^2)\lambda^{\varphi_i^0}_{ZZ}\lambda^{\varphi_i^0}_{H^\pm W^\mp}C_{24}$	$[p_W, -p_{H^\pm}, m_{\varphi_i^0}, m_{H^\pm}, m_Z]$
$G^{4[4]}$	$\frac{g^4 v}{4c_W^3}(c_W^2-s_W^2)\lambda^{\varphi_i^0}_{ZZ}\lambda^{\varphi_i^0}_{H^\pm W^\mp}(-2C_{12}+C_{22}-C_{23})$	$[p_W, -p_{H^\pm}, m_{\varphi_i^0}, m_{H^\pm}, m_Z]$
$F^{4[5]}$	$-\frac{g^4 c_W v}{4}\lambda^{\varphi_i^0}_{W^\pm W^\mp}\lambda^{\varphi_i^0}_{H^\pm W^\mp}[(m_W^2-m_{H^\pm}^2)C_0-\tilde{C}_0$ $-(m_{H^\pm}^2+m_W^2-m_Z^2)C_{11}+2m_{H^\pm}^2C_{12}+C_{24}]$	$[p_W, -p_{H^\pm}, m_{W^\pm}, m_{\varphi_i^0}, m_{W^\pm}]$
$G^{4[5]}$	$-\frac{g^4 c_W v}{4}\lambda^{\varphi_i^0}_{W^\pm W^\mp}\lambda^{\varphi_i^0}_{H^\pm W^\mp}[4(C_0+C_{11})-2C_{12}+C_{22}-C_{23}]$	$[p_W, -p_{H^\pm}, m_{W^\pm}, m_{\varphi_i^0}, m_{W^\pm}]$
$F^{4[6]}$	$\frac{g^4 v}{4c_W}\lambda^{\varphi_i^0}_{ZZ}\lambda^{\varphi_i^0}_{H^\pm W^\mp}[(m_Z^2-m_{H^\pm}^2)C_0-\tilde{C}_0$ $+(m_{H^\pm}^2+m_W^2-m_Z^2)C_{11}-2m_{H^\pm}^2C_{12}+C_{24}]$	$[p_W, -p_{H^\pm}, m_Z, m_{W^\pm}, m_{\varphi_i^0}]$
$G^{4[6]}$	$\frac{g^4 v}{4c_W}\lambda^{\varphi_i^0}_{ZZ}\lambda^{\varphi_i^0}_{H^\pm W^\mp}[4C_0+2(C_{11}+C_{12})+C_{22}-C_{23}]$	$[p_W, -p_{H^\pm}, m_Z, m_{W^\pm}, m_{\varphi_i^0}]$
$F^{4[7]}$	$\frac{g^2 v}{2c_W}(\lambda_4-2\lambda_5)\lambda^{\varphi_i^0}_{AZ}\lambda^{\varphi_i^0}_{G^\pm W^\mp}C_{24}$	$[p_W, -p_{H^\pm}, m_{\varphi_i^0}, m_{W^\pm}, m_A]$
$G^{4[7]}$	$\frac{g^2 v}{2c_W}(\lambda_4-2\lambda_5)\lambda^{\varphi_i^0}_{AZ}\lambda^{\varphi_i^0}_{G^\pm W^\mp}(C_{22}-C_{23})$	$[p_W, -p_{H^\pm}, m_{\varphi_i^0}, m_{W^\pm}, m_A]$
$F^{4[8]}$	$-\frac{g^2 v}{c_W}\lambda^{\varphi_i^0}_{G^0Z}\lambda^{\varphi_i^0}_{G^\pm H^\mp}C_{24}$	$[p_W, -p_{H^\pm}, m_Z, m_{W^\pm}, m_{\varphi_i^0}]$
$G^{4[8]}$	$-\frac{g^2 v}{c_W}\lambda^{\varphi_i^0}_{G^0Z}\lambda^{\varphi_i^0}_{G^\pm H^\mp}(C_{22}-C_{23})$	$[p_W, -p_{H^\pm}, m_Z, m_{W^\pm}, m_{\varphi_i^0}]$
$F^{4[9]}$	$\frac{g^2 v}{c_W}(c_W^2-s_W^2)\lambda^{\varphi_i^0}_{G^\pm H^\mp}\lambda^{\varphi_i^0}_{G^\pm W^\mp}C_{24}$	$[p_W, -p_{H^\pm}, m_{W^\pm}, m_{\varphi_i^0}, m_{W^\pm}]$
$G^{4[9]}$	$\frac{g^2 v}{c_W}(c_W^2-s_W^2)\lambda^{\varphi_i^0}_{G^\pm H^\mp}\lambda^{\varphi_i^0}_{G^\pm W^\mp}(C_{22}-C_{23})$	$[p_W, -p_{H^\pm}, m_{W^\pm}, m_{\varphi_i^0}, m_{W^\pm}]$
$F^{4[10]}$	$\frac{g^4 v^3}{4c_W^3}s_W^2\lambda^{\varphi_i^0}_{G^\pm H^\mp}\lambda^{\varphi_i^0}_{ZZ}C_0$	$[p_W, -p_{H^\pm}, m_Z, m_{W^\pm}, m_{\varphi_i^0}]$
$F^{4[11]}$	$\frac{g^4 v^3}{4c_W}s_W^2\lambda^{\varphi_i^0}_{G^\pm H^\mp}\lambda^{\varphi_i^0}_{W^\pm W^\mp}C_0$	$[p_W, -p_{H^\pm}, m_{W^\pm}, m_{\varphi_i^0}, m_{W^\pm}]$
$F^{4[12]}$	$\frac{g^4 v}{4c_W}s_W^2\lambda^{\varphi_i^0}_{G^\pm W\mp}\lambda^{\varphi_i^0}_{H^\pm W^\mp}C_{24}$	$[p_W, -p_{H^\pm}, m_{W^\pm}, m_{\varphi_i^0}, m_{W^\pm}]$
$G^{4[12]}$	$\frac{g^4 v}{4c_W}s_W^2\lambda^{\varphi_i^0}_{G^\pm W\mp}\lambda^{\varphi_i^0}_{H^\pm W^\mp}(-2C_{12}+C_{22}-C_{23})$	$[p_W, -p_{H^\pm}, m_{W^\pm}, m_{\varphi_i^0}, m_{W^\pm}]$

TABLE III. The F term from the boson-loop diagrams in Fig. 5 contributing to the decay $H^+ \to W^+Z$, where $\mathcal{P} = h, H, A, G^0$ and $\varphi_1^0 = h$, $\varphi_2^0 = H$.

Fig. 5	Amplitude	Argument
$F^{5[1]}_{H^\pm}$	$\frac{g^2 v}{2c_W} s_W^2 \lambda^{\varphi_i^0}_{H^\pm H^\mp} \lambda^{\varphi_i^0}_{H^\pm W^\mp Z} B_0$	$[p_{H^\pm}, m_{\varphi_i^0}, m_{H^\pm}]$
$F^{5[1]}_{G^\pm}$	$\frac{g^2 v}{2c_W} s_W^2 \lambda^{\varphi_i^0}_{G^\pm H^\mp} \lambda^{\varphi_i^0}_{G^\pm W^\mp Z} B_0$	$[p_{H^\pm}, m_{\varphi_i^0}, m_{W^\pm}]$
$F^{5[2]}$	$\frac{g^4 v}{4c_W} s_W^2 \lambda^{\varphi_i^0}_{W^\pm W^\mp} \lambda^{\varphi_i^0}_{H^\pm W^\mp Z} B_0$	$[-p_W, m_{W^\pm}, m_{\varphi_i^0}]$
$F^{5[3]}$	$\frac{g^4 v}{4c_W^3} s_W^2 \lambda^{\varphi_i^0}_{ZZ} \lambda^{\varphi_i^0}_{H^\pm W^\mp Z} B_0$	$[-p_Z, m_{\varphi_i^0}, m_Z]$
$F^{5[4]}$	$-\frac{g^4 c_W v}{4} \frac{m_W^2 - m_Z^2}{m_{H^\pm}^2 - m_W^2} \lambda^{\varphi_i^0}_{W^\pm W^\mp} \lambda^{\varphi_i^0}_{H^\pm W^\mp} (B_0 - B_1)$	$[p_{H^\pm}, m_{\varphi_i^0}, m_{W^\pm}]$
$F^{5[5]}_{H^\pm}$	$-\frac{g^2 c_W v}{2} \frac{m_W^2 - m_Z^2}{m_{H^\pm}^2 - m_W^2} \lambda^{\varphi_i^0}_{H^\pm H^\mp} \lambda^{\varphi_i^0}_{H^\pm W^\mp} (B_0 + 2B_1)$	$[p_{H^\pm}, m_{\varphi_i^0}, m_{H^\pm}]$
$F^{5[5]}_{G^\pm}$	$-\frac{g^2 c_W v}{2} \frac{m_W^2 - m_Z^2}{m_{H^\pm}^2 - m_W^2} \lambda^{\varphi_i^0}_{G^\pm H^\mp} \lambda^{\varphi_i^0}_{G^\pm W^\mp} (B_0 + 2B_1)$	$[p_{H^\pm}, m_{\varphi_i^0}, m_{W^\pm}]$
$F^{5[6]}$	$-\frac{g^4 v}{8c_W} \frac{s_W^2}{m_{H^\pm}^2 - m_W^2} \lambda^{\varphi_i^0}_{G^\pm W^\mp} \lambda^{\varphi_i^0}_{H^\pm W^\mp} (m_{H^\pm}^2 (B_0 - 2B_1) + \tilde{B}_0)$	$[p_{H^\pm}, m_{\varphi_i^0}, m_{W^\pm}]$
$F^{5[7]}_{H^\pm}$	$\frac{g^2 v^3}{2c_W} \frac{s_W^2}{m_{H^\pm}^2 - m_W^2} \lambda^{\varphi_i^0}_{H^\pm H^\mp} \lambda^{\varphi_i^0}_{G^\pm H^\mp} B_0$	$[p_{H^\pm}, m_{\varphi_i^0}, m_{H^\pm}]$
$F^{5[7]}_{G^\pm}$	$\frac{g^2 v^3}{2c_W} \frac{s_W^2}{m_{H^\pm}^2 - m_W^2} \lambda^{\varphi_i^0}_{G^\pm H^\mp} \lambda^{\varphi_i^0}_{G^\pm G^\mp} B_0$	$[p_{H^\pm}, m_{\varphi_i^0}, m_{W^\pm}]$
$F^{5[8]}$	$-\frac{v}{m_{\varphi_i^0}^2} \frac{g^2 s_W^2}{4c_W} \lambda^{\varphi_i^0}_{H^\pm W^\mp Z} [4g^2 \lambda^{\varphi_i^0}_{W^\pm W^\mp} A_0[m_{W^\pm}] + \frac{2g^2}{c_W^2} \lambda^{\varphi_i^0}_{ZZ} A_0[m_Z] + \lambda^{\varphi_i^0}_{\mathcal{P}\mathcal{P}} A_0[m_{\mathcal{P}}] + 2(\lambda^{\varphi_i^0}_{G^\pm G^\pm} A_0[m_{W^\pm}] + \lambda^{\varphi_i^0}_{H^\pm H^\pm} A_0[m_{H^\pm}])]$	
$F^{5[9]}$	$\frac{g^2 v}{c_W} \frac{s_W^2}{m_{H^\pm}^2 - m_{W^\pm}^2} [\lambda_7 (A_0[m_{H^\pm}] + \frac{A_0[m_A]}{4}) + \frac{1}{4} \lambda^{\varphi_i^0 \varphi_i^0}_{G^\pm H^\pm} A_0[m_{\varphi_i^0}] + \lambda_6 (A_0[m_{W^\pm}] + \frac{A_0[m_Z]}{4})]$	
$F^{5[10]}$	$-\frac{g^2 v c_W}{2m_{\varphi_i^0}^2} \frac{m_{W^\pm}^2 - m_Z^2}{m_{H^\pm}^2 - m_{W^\pm}^2} R_{i2} [-2g^2 \lambda^{\varphi_i^0}_{W^\pm W^\mp} A_0[m_{W^\pm}] - \frac{g^2}{c_W^2} \lambda^{\varphi_i^0}_{ZZ} A_0[m_Z] - \frac{1}{2} \lambda^{\varphi_i^0}_{\mathcal{P}\mathcal{P}} A_0[m_{\mathcal{P}}] - (\lambda^{\varphi_i^0}_{G^\pm G^\pm} A_0[m_{W^\pm} + \lambda^{\varphi_i^0}_{H^\pm H^\pm} A_0[m_{H^\pm}])]$	
$F^{5[11]}$	$\frac{g^2 v^3}{2c_W} \frac{s_W^2}{m_{H^\pm}^2 - m_{W^\pm}} \frac{1}{m_{\varphi_i^0}^2} [2g^2 \lambda^{\varphi_i^0}_{W^\pm W^\mp} A_0[m_{W^\pm}] + \frac{g^2}{c_W^2} \lambda^{\varphi_i^0}_{ZZ} A_0[m_Z] + \frac{1}{2} \lambda^{\varphi_i^0}_{\mathcal{P}\mathcal{P}} A_0[m_{\mathcal{P}}] + (\lambda^{\varphi_i^0}_{G^\pm G^\pm} A_0[m_{W^\pm} + \lambda^{\varphi_i^0}_{H^\pm H^\pm} A_0[m_{H^\pm}])]$	

TABLE IV. The F, G, and H term from the fermion-loop diagrams in Fig. 6 contributing to the decay $H^+ \to W^+ Z$, with $\varphi_1^0 = h$ and $\varphi_2^0 = H$. Here, u represents all the up-type quarks, and d represents the down-type quarks and the fermions.

Fig. 6	Amplitude	Argument
$F^{6[1]}$	$-\frac{2N_C g^2 c_W}{v}\frac{m_Z^2-m_{W^\pm}^2}{m_{H^\pm}^2-m_{W^\pm}^2}\lvert V_{ud}\rvert^2\{m_d^2\varsigma_d(B_1+B_0)-m_u^2\varsigma_u B_1\}$	$[p_{H^\pm}, m_d, m_u]$
$F^{6[2]}$	$\frac{2N_C g^2}{vc_W}\lvert V_{ud}\rvert^2\{m_d^2(g_V^d-g_A^d)(\frac{\varsigma_d}{2}(m_{H^\pm}^2-m_{W^\pm}^2-m_Z^2)+m_u^2\varsigma_u)C_0$ $+(2g_A^d m_d^2\varsigma_d-(g_A^d+g_V^d)m_u^2\varsigma_u)\tilde{C}_0$ $-\frac{1}{2}(g_A^d(m_d^2\varsigma_d-m_u^2\varsigma_u)-g_V^d(m_d^2\varsigma_d+m_u^2\varsigma_u))$ $((m_{H^\pm}^2-m_{W^\pm}^2-m_Z^2)C_{11}-(m_{H^\pm}^2-m_{W^\pm}^2+m_Z^2)C_{12})$ $+2g_A^d m_d^2\varsigma_d(m_{W^\pm}^2C_{11}-\frac{1}{2}(m_{H^\pm}^2+m_{W^\pm}^2-m_Z^2)C_{12})$ $-2(g_A^d+g_V^d)(m_d^2\varsigma_d-m_u^2\varsigma_u)C_{24}\}$	$[p_W, -p_{H^\pm}, m_d, m_u, m_d]$
$G^{6[2]}$	$\frac{2N_C g^2}{vc_W}\lvert V_{ud}\rvert^2\{m_d^2\varsigma_d(g_A^d-g_V^d)(C_0+C_{11})-m_u^2\varsigma_u(g_A^d+g_V^d)C_{11}$ $+(g_A^d+g_V^d)((m_d^2\varsigma_d+m_u^2\varsigma_u)C_{12}-2(m_d^2\varsigma_d-m_u^2\varsigma_u)(C_{22}-C_{23}))\}$	$[p_W, -p_{H^\pm}, m_d, m_u, m_d]$
$H^{6[2]}$	$\frac{2N_C g^2}{vc_W}\lvert V_{ud}\rvert^2\{m_d^2\varsigma_d(g_A^d-g_V^d)(C_0+C_{11})+m_u^2\varsigma_u(g_A^d+g_V^d)C_{11}$ $+(g_A^d+g_V^d)(m_d^2\varsigma_d-m_u^2\varsigma_u)C_{12}\}$	$[p_W, -p_{H^\pm}, m_d, m_u, m_d]$
$F^{6[3]}$	$\frac{2N_C g^2}{vc_W}\lvert V_{ud}\rvert^2\{m_u^2(g_A^u-g_V^u)(m_d^2\varsigma_d+\frac{\varsigma_u}{2}(m_{H^\pm}^2-m_{W^\pm}^2-m_Z^2))C_0$ $+(m_d^2\varsigma_d(g_A^u+g_V^u)-2m_u^2\varsigma_u g_A^u)\tilde{C}_0$ $-\frac{1}{2}(m_d^2\varsigma_d(g_A^u+g_V^u)-m_u^2\varsigma_u(g_A^u-g_V^u))$ $((m_{H^\pm}^2-m_{W^\pm}^2-m_Z^2)C_{11}-(m_{H^\pm}^2-m_{W^\pm}^2+m_Z^2)C_{12})$ $-2g_A^u m_u^2\varsigma_u(m_{W^\pm}^2C_{11}-\frac{1}{2}(m_{H^\pm}^2+m_{W^\pm}^2-m_Z^2))C_{12})$ $-2(g_A^u+g_V^u)(m_d^2\varsigma_d-m_u^2\varsigma_u)C_{24}\}$	$[p_W, -p_{H^\pm}, m_u, m_d, m_u]$
$G^{6[3]}$	$\frac{2N_C g^2}{vc_W}\lvert V_{ud}\rvert^2\{m_u^2\varsigma_u(g_V^u-g_A^u)(C_0+C_{11})+m_d^2\varsigma_d(g_A^u+g_V^u)C_{11}$ $-(g_A^u+g_V^u)((m_d^2\varsigma_d+m_u^2\varsigma_u)C_{12}+2(m_d^2\varsigma_d-m_u^2\varsigma_u)(C_{22}-C_{23}))\}$	$[p_W, -p_{H^\pm}, m_u, m_d, m_u]$
$H^{6[3]}$	$\frac{2N_C g^2}{vc_W}\lvert V_{ud}\rvert^2\{m_u^2\varsigma_u(g_A^u-g_V^u)(C_0+C_{11})+m_d^2\varsigma_d(g_A^u+g_V^u)C_{11}$ $-(g_A^u+g_V^u)((m_d^2\varsigma_d-m_u^2\varsigma_u)C_{12})\}$	$[p_W, -p_{H^\pm}, m_u, m_d, m_u]$
$F^{6[4]}$	$-\frac{2N_C g^2}{vc_W}\frac{s_W^2}{m_{H^\pm}^2-m_{W^\pm}^2}\lvert V_{ud}\rvert^2\{(m_d^2\varsigma_d+m_u^2\varsigma_u)(m_{H^\pm}^2B_1+\tilde{B}_0)$ $-m_u^2m_d^2(\varsigma_u+\varsigma_d)B_0\}$	$[p_{H^\pm}, m_d, m_u]$
$F^{6[5]}$	$\frac{6}{m_{\varphi_i^0}^2}\frac{g^2s_W^2}{vc_W}\lambda_{H^\pm W^\mp Z}^{\varphi_i^0}\sum_{f=u,d}(m_f^2\lambda_{f\bar{f}}^{\varphi_i^0}A_0)$	$m_{u,d}$
$F^{6[6]}$	$\frac{6}{m_{\varphi_i^0}^2}\frac{g^2c_W}{v}\frac{m_Z^2-m_W^2}{m_{H^\pm}^2-m_W^2}\lambda_{H^\pm W^\mp}^{\varphi_i^0}\sum_{f=u,d}(m_f^2\lambda_{f\bar{f}}^{\varphi_i^0}A_0)$	$m_{u,d}$
$F^{6[7]}$	$\frac{6}{m_{\varphi_i^0}^2}\frac{g^2vs_W^2}{c_W}\frac{1}{m_{H^\pm}^2-m_W^2}\lambda_{H^\pm G^\mp}^{\varphi_i^0}\sum_{f=u,d}(m_f^2\lambda_{f\bar{f}}^{\varphi_i^0}A_0)$	$m_{u,d}$

the appendix of Ref. [67]. The integration measure in D dimensions is given by

$$d^D\tilde{k} = \mu^{3(4-D)/2}\frac{d^Dk}{(2\pi)^D}, \tag{B1}$$

where $g\mu^{(4-D)/2}$ is the $\mathrm{SU}(2)_L$ gauge coupling constant in D dimensions. The scalar-loop functions appearing are given by [68,69]

$$A_0(m_1) = \int d^D\tilde{k}\frac{1}{k^2 - m_1^2},$$
$$B_0(l, m_1, m_2) = \int d^D\tilde{k}\frac{1}{(k^2 - m_1^2)[(k+l)^2 - m_2^2]},$$
$$C_0(l, s, m_1, m_2, m_3) = \int d^D\tilde{k}\frac{1}{(k^2 - m_1^2)[(k+l)^2 - m_2^2][(k+l+s)^2 - m_3^2]}. \tag{B2}$$

We use the definitions $s_1 = l^2 + m_1^2 - m_2^2$ and $s_2 = s^2 + 2l\cdot s + m_2^2 - m_3^2$ following Ref. [67]. The loop functions are given by

$$\tilde{B}_0 = A_0(m_2) + m_1^2 B_0, \qquad B_1 = \frac{1}{2l^2}[A_0(m_1) - A_0(m_2) - s_1 B_0], \qquad \tilde{C}_0 = B_0(s, m_2, m_3) + m_1^2 C_0, \tag{B3}$$

$$\begin{aligned} C_{22} &= \frac{1}{2[l^2s^2 - (ls)^2]}\{-ls[B_1(l+s, m_1, m_3) - B_1(s, m_2, m_3) - s_1 C_{12}] \\ &\quad + l^2[-B_1(l+s, m_1, m_3) - s_2 C_{12} - 2C_{24}]\}, \\ C_{24} &= \frac{1}{2(D-2)}[1 + B_0(s, m_2, m_3) + 2m_1^2 C_0 + s_1 C_{11} + s_2 C_{12}]. \end{aligned} \tag{B4}$$

$$\begin{aligned} \begin{pmatrix} C_{11} \\ C_{12} \end{pmatrix} &= \frac{1}{2}\mathcal{X}\begin{bmatrix} B_0(l+s, m_1, m_3) - B_0(s, m_2, m_3) - s_1 C_0 \\ B_0(l, m_1, m_2) - B_0(l+s, m_1, m_3) - s_2 C_0 \end{bmatrix}, \\ \begin{pmatrix} C_{21} \\ C_{23} \end{pmatrix} &= \frac{1}{2}\mathcal{X}\begin{bmatrix} B_1(l+s, m_1, m_3) + B_0(s, m_2, m_3) - s_1 C_{11} - 2C_{24} \\ B_1(l, m_1, m_2) - B_1(l+s, m_1, m_3) - s_2 C_{11} \end{bmatrix}, \end{aligned} \tag{B5}$$

with

$$\mathcal{X} = \frac{1}{[l^2s^2 - (ls)^2]}\begin{bmatrix} s^2 & -ls \\ -ls & l^2 \end{bmatrix}. \tag{B6}$$

[1] J. F. Gunion, H. E. Haber, G. L. Kane, and S. Dawson, Front. Phys. **80**, 1 (2000).
[2] G. C. Branco, P. M. Ferreira, L. Lavoura, M. N. Rebelo, M. Sher, and J. P. Silva, Phys. Rep. **516**, 1 (2012).
[3] N. Turok and J. Zadrozny, Nucl. Phys. **B358**, 471 (1991).
[4] M. Hashimoto and S. Kanemura, Phys. Rev. D **70**, 055006 (2004); **70**, 119901(E) (2004).
[5] A. Zee, Phys. Lett. **93B**, 389 (1980); **95B**, 461(E) (1980).
[6] S. Heinemeyer *et al.*, arXiv:hep-ph/0511332.
[7] A. G. Akeroyd *et al.*, Eur. Phys. J. C **77**, 276 (2017).
[8] R. Godbole, B. Mukhopadhyaya, and M. Nowakowski, Phys. Lett. B **352**, 388 (1995).
[9] P. Bandyopadhyay, K. Huitu, and A. Sabanci Keceli, J. High Energy Phys. 05 (2015) 026.
[10] P. Bandyopadhyay, C. Corian, and A. Costantini, Phys. Rev. D **94**, 055030 (2016).
[11] P. Bandyopadhyay and A. Costantini, J. High Energy Phys. 01 (2018) 067.
[12] J. A. Grifols and A. Mendez, Phys. Rev. D **22**, 1725 (1980).
[13] T. G. Rizzo, Mod. Phys. Lett. A **04**, 2757 (1989).
[14] M. Capdequi Peyranere, H. E. Haber, and P. Irulegui, Phys. Rev. D **44**, 191 (1991).
[15] S. Kanemura, Phys. Rev. D **61**, 095001 (2000).
[16] S. Kanemura, Eur. Phys. J. C **17**, 473 (2000).
[17] S. Moretti, D. Rojas, and K. Yagyu, J. High Energy Phys. 08 (2015) 116.
[18] J. L. Diaz-Cruz, J. Hernandez-Sanchez, and J. J. Toscano, Phys. Lett. B **512**, 339 (2001).
[19] A. Arhrib, R. Benbrik, and M. Chabab, J. Phys. G **34**, 907 (2007).
[20] S. L. Glashow and S. Weinberg, Phys. Rev. D **15**, 1958 (1977).
[21] E. A. Paschos, Phys. Rev. D **15**, 1966 (1977).
[22] A. Pich and P. Tuzon, Phys. Rev. D **80**, 091702 (2009).
[23] M. Jung, A. Pich, and P. Tuzon, J. High Energy Phys. 11 (2010) 003.

[24] M. Jung, X.-Q. Li, and A. Pich, J. High Energy Phys. 10 (2012) 063.
[25] A. Celis, M. Jung, X.-Q. Li, and A. Pich, J. High Energy Phys. 01 (2013) 054.
[26] M. Jung and A. Pich, J. High Energy Phys. 04 (2014) 076.
[27] M. Jung, A. Pich, and P. Tuzon, Phys. Rev. D **83**, 074011 (2011).
[28] X.-Q. Li, J. Lu, and A. Pich, J. High Energy Phys. 06 (2014) 022.
[29] W. Dekens, J. de Vries, J. Bsaisou, W. Bernreuther, C. Hanhart, Ulf-G. Meißner, A. Nogga, and A. Wirzba, J. High Energy Phys. 07 (2014) 069.
[30] W. Altmannshofer, S. Gori, and G. D. Kribs, Phys. Rev. D **86**, 115009 (2012).
[31] Y. Bai, V. Barger, L. L. Everett, and G. Shaughnessy, Phys. Rev. D **87**, 115013 (2013).
[32] A. Celis, V. Ilisie, and A. Pich, J. High Energy Phys. 07 (2013) 053.
[33] V. Barger, L. L. Everett, H. E. Logan, and G. Shaughnessy, Phys. Rev. D **88**, 115003 (2013).
[34] D. Lopez-Val, T. Plehn, and M. Rauch, J. High Energy Phys. 10 (2013) 134.
[35] L. Duarte, G. A. Gonzalez-Sprinberg, and J. Vidal, J. High Energy Phys. 11 (2013) 114.
[36] A. Celis, V. Ilisie, and A. Pich, J. High Energy Phys. 12 (2013) 095.
[37] L. Wang and X. F. Han, J. High Energy Phys. 04 (2014) 128.
[38] G. Abbas, A. Celis, X. Q. Li, J. Lu, and A. Pich, J. High Energy Phys. 06 (2015) 005.
[39] T. Enomoto and R. Watanabe, J. High Energy Phys. 05 (2016) 002.
[40] Q. Y. Hu, X. Q. Li, and Y. D. Yang, Eur. Phys. J. C **77**, 190 (2017).
[41] S. Gori, H. E. Haber, and E. Santos, J. High Energy Phys. 06 (2017) 110.
[42] A. Penuelas and A. Pich, J. High Energy Phys. 12 (2017) 084.
[43] G. Aad *et al.* (ATLAS Collaboration), Phys. Lett. B **716**, 1 (2012).
[44] S. Chatrchyan *et al.* (CMS Collaboration), Phys. Lett. B **716**, 30 (2012).
[45] G. Aad *et al.* (ATLAS and CMS Collaborations), J. High Energy Phys. 08 (2016) 045.
[46] V. Khachatryan *et al.* (CMS Collaboration), Eur. Phys. J. C **75**, 212 (2015).
[47] I. F. Ginzburg and I. P. Ivanov, Phys. Rev. D **72**, 115010 (2005).
[48] F. Staub, Phys. Lett. B **776**, 407 (2018).
[49] M. D. Goodsell and F. Staub, Eur. Phys. J. C **78**, 649 (2018).
[50] M. D. Goodsell and F. Staub, arXiv:1805.07310.
[51] M. E. Peskin and T. Takeuchi, Phys. Rev. D **46**, 381 (1992).
[52] (ALEPH, DELPHI, L3, and OPAL Collaborations and LEP Higgs Working Group for Higgs Boson Searches), arXiv: hep-ex/0107031.
[53] CMS Collaboration, Report No. CMS-PAS-HIG-16-031.
[54] ATLAS Collaboration, Report No. ATLAS-CONF-2016-088.
[55] ATLAS Collaboration, Report No. ATLAS-CONF-2016-089.
[56] A. M. Sirunyan *et al.* (CMS Collaboration), Phys. Rev. Lett. **119**, 141802 (2017).
[57] J. Alwall, M. Herquet, F. Maltoni, O. Mattelaer, and T. Stelzer, J. High Energy Phys. 06 (2011) 128.
[58] R. Mertig, M. Bohm, and A. Denner, Comput. Phys. Commun. **64**, 345 (1991).
[59] V. Shtabovenko, R. Mertig, and F. Orellana, Comput. Phys. Commun. **207**, 432 (2016).
[60] A. Alloul, N. D. Christensen, C. Degrande, C. Duhr, and B. Fuks, Comput. Phys. Commun. **185**, 2250 (2014).
[61] T. Hahn, Comput. Phys. Commun. **140**, 418 (2001).
[62] T. Hahn and M. Perez-Victoria, Comput. Phys. Commun. **118**, 153 (1999).
[63] E. Asakawa and S. Kanemura, Phys. Lett. B **626**, 111 (2005).
[64] G. Apollinari, O. Brning, T. Nakamoto, and L. Rossi, CERN Yellow Report No. 5, 2015, DOI: 10.5170/CERN-2015-005.1.
[65] C. W. Chiang and K. Yagyu, J. High Energy Phys. 01 (2013) 026.
[66] M. Zaro and H. Logan (LHC Higgs Cross Section Working Group), Report No. LHCHXSWG-2015-001.
[67] A. Axelrod, Nucl. Phys. **B209**, 349 (1982).
[68] G. 't Hooft and M. J. G. Veltman, Nucl. Phys. **B153**, 365 (1979).
[69] G. Passarino and M. J. G. Veltman, Nucl. Phys. **B160**, 151 (1979).